MULTI-CHAMBER CYLINDRICAL OSCILLATING WATER COLUMN WAVE ENERGY HARVESTERS: SEMI-ANALYTICAL MODELING AND PERFORMANCE ANALYSIS

A Thesis Submitted in Partial Fulfilment of the Requirements
for the Degree of Doctor of Philosophy in

Sustainable Development and Climate change

Doctoral Programme of National Interest

PhD SDC
SUSTAINABLE DEVELOPMENT
AND CLIMATE CHANGE

In the Curriculum
TECHNOLOGY AND TERRITORY

Ing. Antonino Simone Spanò

01, 2025

MULTI-CHAMBER CYLINDRICAL OSCILLATING WATER COLUMN WAVE ENERGY HARVESTERS: SEMI-ANALYTICAL MODELING AND PERFORMANCE ANALYSIS

A Thesis Submitted in Partial Fulfilment of the Requirements
for the Degree of Doctor of Philosophy in

Sustainable Development and Climate change

Doctoral Programme of National Interest

PhD SDC
SUSTAINABLE DEVELOPMENT
AND CLIMATE CHANGE

In the Curriculum
TECHNOLOGY AND TERRITORY

by

Ing. Antonino Simone Spanò

Supervisor: Prof. Ing. Felice Arena

Co-Supervisor: Prof. Ing. Giovanni Malara

ABSTRACT

Wave energy is widely recognized for its global availability and intensity to have the potential to meet the world's energy demand. Several devices have been designed to harvest this energy source: while some have been developed at full scale, few have been adopted in industry. The lack of convergence toward a single standardized device has not promoted its widespread deployment. However, a general consensus has been achieved on Oscillating Water Columns, that have been implemented in a variety of scenarios. This work considers the energy production of a circular device equipped with Oscillating Water Column (OWC) technology for harnessing wave energy.

A semi-analytical solution of a related linear potential flow problem represented through the expansion of eigenfunctions and solved using the matching technique has been developed. This approach allowed examining the relevance of the device geometric parameters and their influence on the overall system performance. The parametric studies on the angular width of the internal chamber promoted the further analysis of vertical cylinders incorporating multiple OWC chambers having a reduced angular width. The critical characteristic of the proposed OWC concept is that the OWC chambers are arranged on the same circular ring, in contrast to the multi-chamber OWCs modelled as concentric rings commonly found in literature. A case study at the location of Mazara del Vallo (Italy) summarizes the considerations presented in previous chapters, showing a preliminary study on the energy that can be produced.

Overall, the semi-analytical solution tends to overestimate the results, as it neglects the effects of non-linearity or viscosity. However, it provides a rapid and comprehensive preliminary analysis of the case under study, offering a consistent basis for more detailed investigations.

ACKNOWLEDGEMENTS

Acknowledgements can be provided here (though it is not compulsory to include them).

TABLE OF CONTENTS

LIST OF FIGURES

LIST OF TABLES

CHAPTER 1

Introduction

1 INTRODUCTION

1.1 GENERAL REMARKS

Climate change holds a central position in modern global discussion. Current generations are born into the reality of this condition, characterized by global warming, increasingly frequent extreme natural events, air quality pollution, rising sea levels and so on. These effects require urgent action to address consequences affecting the whole of humanity. Since the Industrial Revolution, energy production has fueled the release of greenhouse gases (GHG) into the atmosphere. Today, the energy sector is responsible for approximately 70% of global GHG emissions. Over recent decades, technological advances have led to an exponential dependency on electricity. As a result, among the various measures needed to fight climate change, a transformation in electricity production is particularly essential.

The transition to renewable energy sources has seen significant development in exploiting natural resources such as solar, wind, and hydropower. Each resource presents notable advantages and disadvantages, such as predictability, environmental impact and energy density distribution. Building an energy mix is emerging as the strategic solution to meet the growing global demand. Among the planet's natural resources, the oceans, covering up to 70% of the Earth's surface, contain a remarkable energy potential, capable of meeting global energy demand through vast spaces and diverse sources of energy. Multiple methods exist to extract energy from the oceans, including tidal, current, wave, thermal gradient, and salinity gradient exploitation.

This work focuses on the devices harvesting energy from sea waves. Wave energy is harvested mainly via devices exploiting three operating principles: oscillating bodies (OBs), overtopping devices (OTDs), and Oscillating Water Column (OWC) systems. OWC technology proves to be the most reliable, promising, and productive. The working principle is based on a water column within the device, activated by the wave motion through an opening at its base. The oscillation of the water column causes compression and expansion of the air chamber above it, which generates an airflow through an opening at the top of the chamber. By placing a turbine at this outlet, the bidirectional airflow can be harnessed to produce electricity. The absence of moving parts in water is an advantage against the cyclical and periodic stresses of wave motion. Moreover, this technology can be easily integrated into existing structures, operating in both onshore and offshore environments, whether in fixed or floating

installations, transforming them from passive to active systems capable of converting wave energy.

This thesis examines a generic floating vertical circular structure in deep waters, equipped with an internal chamber for wave energy conversion. An internal cylinder connects a disc to the base of the device, improving stability and buoyancy conditions. The advantage of circular shape lies in its independence from the wave direction when evaluating the interaction with the structure. This form is widely used in both offshore and onshore structures, in deep and shallow waters. The main applications include industrial platforms, offshore wind energy (both fixed and floating), aquaculture facilities, and more. Compared to other studies in the literature, particular attention is given to the angular width of the internal chamber, analyzing the effects of a chamber spanning a reduced portion of the circular sector. The thesis is divided into two main parts, focusing on the study of two types of cylindrical OWC concepts: single-chamber and multi-chamber, showed in Figure 1. In the first case, a series of parametric investigations are conducted to analyze the influence on the device's performance. In the second case, the focus is on the constructive or destructive effects arising from the presence of multiple chambers and the potential advantages or disadvantages compared to a single-chamber structure.

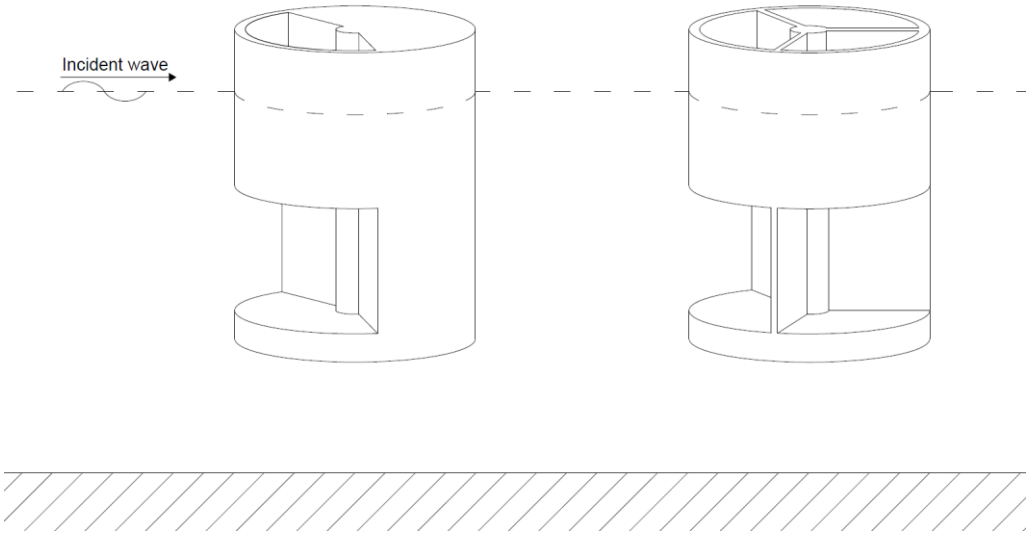

Figure 1 –Circular OWC concept investigated. 3D view: single-chamber (left), multi-chamber (right).

All these analyses are developed through the formulation of an analytical model, based on potential flow theory, employing the eigenfunction expansion method and matching technique. The objective of this thesis is to investigate the performance of cylindrical OWC devices and analyze the effects of its geometric parameters on the overall system performance, in order to optimize the overall energy production of these devices, while providing also practical recommendations for optimal design solutions.

1.2 RESEARCH APPROACH

The aim of this study is to develop a semi-analytical solution to investigate the contribution of the main geometric parameters of a circular OWC device, with the goal of enhancing energy productivity.

Among the various methods for analyzing wave-structure interaction, a semi-analytical approach has been adopted, particularly suitable for the early design stages of an OWC device. By neglecting viscosity effects and assuming an incompressible fluid with irrotational motion, a velocity potential can be introduced to describe the kinematic conditions. The domain is divided into subdomains, and the potential is derived for each one using boundary conditions and eigenfunctions expansions with unknown coefficients. Unknowns are determined through the matching technique, which enforces continuity of pressure and velocity across the interfaces of contiguous domains. Neglecting nonlinear effects allows the application of the superposition principle, enabling separate analyses of the diffracted and radiated wave fields. The former is generated by the interaction of incident waves with the structure, while the latter arises from the motion of the structure or the internal water column acting as a source of radiation. An additional benefit of working within the linear framework is the formulation of a linear power take-off system.

Cylindrical devices are advantageous because they can harness wave energy regardless of wave direction. However, this assumption has been challenged by studying the effects of chambers with reduced angular sectors. Following the results achieved by the single-chamber OWC, this thesis presents a novel concept of multi-chamber configurations. While modern studies have focused on devices with multiple concentric rings, this thesis suggests a different multi-chamber concept: reducing the angular width of individual chambers to accommodate multiple chambers on a single circular ring, thereby optimizing energy production.

The analyses conducted also aim to provide general guidelines for the design phase of a circular OWC. To this purpose, an application case is presented, in which the previously introduced concepts are applied, demonstrating how appropriate methods can optimize the energy production of the device.

1.3 STRUCTURE OF THE THESIS

This work starts with the contextualization of climate change and the urgent need for energy transition and concludes with the presentation of a circular OWC device for clean wave energy production, contributing to the tangible reduction of atmospheric emissions.

Chapter 2 describes the climate change problem and various strategies for climate change mitigation and adaptation. It presents the main renewable energy sources, with a particular focus on ocean energy. The devices designed to harness the wave energy are then explored in detail, with an emphasis on their operating principles and real-scale implementations.

Chapter 3 lays out the mathematical foundations adopted in the subsequent chapters. It outlines the essential steps for the analytical modeling of a circular OWC device. The potential flow theory is introduced, showing the derivation of the velocity potential for circular structures through the proper formulation of boundary conditions and the eigenfunctions expansion technique. The unknown terms are determined using the matching technique, which is explained alongside a simple practical example. The linear modeling of the power take-off system follows.

Chapter 4 examines a vertical cylinder equipped with an internal chamber. After providing an overview of the state of the art for such devices, the analytical solution derived for the case under study is presented. Subsequent analyses explore the contribution of the main geometric parameters to energy productivity.

Chapter 5 addresses the concept of multi-chamber systems from a novel perspective compared to existing scientific literature. The approach is based on the use of chambers with reduced angular width arranged along a single circular ring, rather than in concentric rings. Specifically, two cases of vertical cylinders equipped with two and three chambers are investigated. A comparison with the single-chamber case is also provided.

Chapter 6 briefly presents a practical application for the design of a cylindrical OWC. The device is supposed to be installed in the site of Mazara del Vallo. Based on an analysis of local wave climate data, the optimal geometric configuration of the device is identified, and the energy production of the device is determined.

Chapter 7 concludes the thesis by summarizing the aim of the research, the methodology, the obtained results, as well as the limitations and future perspective of this work.

CHAPTER 2

Wave Energy within Climate Change

Avoiding a global temperature rise above 2°C is the shared goal of 197 nations that signed the Paris Agreement in 2015. Transitioning to clean energy sources is essential to reducing greenhouse gas emissions. Among the various renewable energy sources, the ocean offers a wide range of possibilities. Covering 70% of the Earth's surface, with high predictability and the highest energy density, wave energy has the potential to contribute significantly to global energy.

This chapter provides an introduction to climate change, addressing its causes, effects, and the strategies implemented for mitigation and adaptation. It also presents an overview of the main renewable energy sources, with a specific focus on wave energy technologies and the devices developed to harness it.

2 WAVE ENERGY WITHIN CLIMATE CHANGE

2.1 CLIMATE CHANGE

Climate change refers to long-term shifts in temperatures and weather patterns. Since the 1800s, human activities have become the main driver of climate change, due to the combustion of fossil fuel like coal, oil and gas. This process release greenhouse gases (GHG), generating a blanket around the Earth, trapping the heat from the sun and causing global temperature to rise. These emissions are generated worldwide, although some nations produce more than others as reported by the United Nations (China, USA, India, UE, Russia, Brazil).

Since 1950, effects of climate change have become increasingly evident, especially in terms of extreme events. Precipitations occurrences are becoming shorter and more intense, exceeding the natural human-made drainage systems and leading to damaging floods. Drought periods are growing longer. Each summer is marked as the hottest on record. Ice melting causes sea level rising, posing a threat to the population living in coastal areas. Dry vegetation creates ideal conditions for wildfires. Warming of ocean affects the intensity of hurricanes and typhoons. Many of these events happen in combination with others, increasing the damage and affecting the safety of the population.

Addressing climate change requires a dual approach: mitigation and adaptation. Mitigating climate change means reducing the levels of greenhouse gases into the atmosphere. Climate scientists have demonstrated that in order to avoid the most severe impacts of climate change, global temperatures must be kept below 1.5°C above pre-industrial levels. According to the Paris Agreement signed by 197 nations in 2015, emissions need to be reduced by 45% by 2030 and reach net zero by 2050, to limit global temperature rise to no more than 2°C. In order to achieve this goal, it's necessary to promote alternative source of clean energy, considering that fossil fuels are the large contributor to global climate change, accounting for over the 70% of GHG emissions. In addition to taking all possible measures to reduce the emissions and global warming, it is also necessary to adapt to the inevitable impacts of climate change, becoming more resilient. National governments must manage the country development plan embedding several actions against climate vulnerability, such as

building flood defences, improving water management, planning the land use, investing in energy and public infrastructures.

In order to tackle this global challenge, a worldwide common strategy needs to be taken into account. The Intergovernmental Panel on Climate Change (IPCC) was established by the United Nations Environment Programme (UNEP) and the World Meteorological Organization (WMO) in 1988. The IPCC was established to offer policymakers regular scientific assessments report (AR) on climate change, its impacts, potential future risks, and to propose options for adaptation and mitigation. The Sixth Assessment Report (AR6) has been published in March 2023, summarizing the current understanding of climate change, its impacts and risks, and worldwide mitigation and adaptation strategies. Another central role in the global fight against climate change is played by the United Nations Framework Convention on Climate Change (UNFCC). The 198 countries that have ratified the Convention are called Parties to the Convention and are represented at the Conference of the Parties (COP). COP have grown exponentially over the past two decades. Significant achievements have been made by the UNFCCC, such as the signing of the Kyoto Protocol during COP3 (adopted on 11 December 1997 and effective from 16 February 2005) and the Paris Agreement during COP21 (adopted on 12 December 2015 and entered into force on 4 November 2016).

2.2 RENEWABLE ENERGY

Energy production plays a central role in climate change. Up to 70% of GHG emissions are originated by the use of fossil fuels for energy generation. Transitioning to renewable energy is the only valuable path to reach the goals set by the Paris Agreement. As defined by the United Nations, renewable energy is energy derived from natural sources that are replenished at a higher rate than they are consumed. Despite fossil fuels, green resources are available worldwide, allowing countries also to reduce energy import dependency, promoting an inclusive economic growth. They are classified into six main categories, based on the underlying natural resource.

2.2.1 Bioenergy

Bioenergy is considered a form of renewable energy derived from biomass (organic materials), particularly through the utilization of agricultural, agro-industrial, plant and wood residues. Is mainly divided into two categories: traditional (combustion of wood, animal waste) and modern (biofuel, biogas).

The application of bioenergy includes heat production, with scales ranging from home cooking to large district heating systems; power generation from biomass via combustion; and first-generation liquid biofuels from oil crops (biodiesel) and starch crops (ethanol) (Chum et al., 2011). Bioenergy plays a significant role in most energy scenarios, meeting the need for baseload electrical power, fuels with high energy density and carbon negative energy source (referring to bioenergy with carbon capture storage BECCS) (Reid et al., 2020).

2.2.2 Solar Energy

Solar energy constitutes the thermal radiation emitted by the Sun, reaching the Earth's surface with a magnitude of solar irradiance at sea level of 1000 $\mathrm{W/m^2}$, in clear sky conditions and within a few hours of noon (Arvizu et al., 2011). Two main technologies are used for harnessing solar energy: Photovoltaics (PV) and Concentrating Solar Power (CSP).

PV cells produce electricity by absorbing photons and releasing electrons in form of current, thanks to the conductive properties of materials like silicon through the photoelectric effect. CSP, on the other hand, uses reflectors to concentrate sunlight onto a small area to produce steam, which powers a thermal electric plant (detailed further below). Beyond electricity generation, solar energy is also utilized to produce thermal energy for heating or cooling, either through passive or active systems (Lange, 2013).

In recent years, the market has experienced significant growth, driven by technological advancements and price reductions. Another significant trend is the integration of energy storage solutions with solar system, thanks to the progresses made in battery technologies, such as lithium-ion battery, to store excess solar energy to be used during nighttime (Khare et al., 2023). Solar irradiation is highly dependent on the geographical location and also weather conditions. One of the main challenges is the availability of space: the development of floating offshore photovoltaic farms. This emerging concept

is finding great developments due to the land occupation and also for the cooling systems (DU HONG and Le, 2021).

2.2.3 Geothermal Energy

Geothermal energy is a renewable energy in form of heat, produced and stored beneath the ground. The temperature difference between the surface and those underground storage is known as Geothermal Gradient. It is the source of energy. Worldwide distribution of geothermal resources is mainly focused in three areas: the first is called the Ring of Fire, encompassing the lands surrounding the Pacific Ocean, including the western coasts of the Americas and the eastern coasts of Asia and Australia, accounting the majority of world's geothermal resource. The second zone spans the ocean above Iceland. The third zone extends from the Mediterranean to the Himalayan (Sharmin et al., 2023).

The most common method of harnessing geothermal energy involves drilling directly into underground reservoirs of hot water and steam and pumping them to the surface. The extracted heat is then used for heating and energy generation in buildings such as homes and offices (DiPippo, 2015). Future developments in geothermal energy may include technological advancements to reduce drilling cost.

2.2.4 Hydropower

Hydropower is one of the most efficient renewable energy sources, offering a higher conversion efficiency compared to other renewables. Through a structure, whether a dam or a generic diversion, water is channelled. Its potential energy is harnessed and converted into kinetic energy using change in elevation through a pipeline. The hydro turbine is the core component of a hydropower plant, and the operation and maintenance of its various parts are crucial for achieving optimal energy generation. The water flows through some guide and reaches the blade of the turbine, producing electricity from the kinetic energy. The main turbine used are Pelton, Francis and Kaplan turbine, characterized by an efficiency up to 90% (Kumar and Saini, 2022).

Hydropower is the principal renewable source worldwide, providing in 2020 up to 4000 TWh/year globally generated (Silva and Castillo, 2021). Huge

hydropower plants need up to 10-20 years to be constructed, requiring complex design and development. The construction of large hydropower plants has a significant impact on the social, economic, and natural environment. These structures modify downstream ecosystems, alter the landscape, and affect local flora and fauna.

2.2.5 Ocean Energy

World's oceans are abundant sources of different forms of renewable energy, such as tides, currents, waves, thermal gradient and salinity gradient. Some of the main advantages, compared to other renewable energy sources are its consistency, predictability and wide availability (Hussain et al., 2017).

Tidal and current energy is generated by the regular movement of tides due to the gravitational force from the Sun and the Moon against the Earth. Tidal energy is harnessed through its potential energy, throughout tidal barrage, its working principle is similar to hydropower systems. Current energy is utilized in the form of kinetic energy. Current Energy Converters are designed following the principles of wind turbine systems, both horizontal and vertical axis, deployed underwater (Li and Zhu, 2023).

Waves are generated by the wind blowing over the water surface. Height and period of the waves, depends on the energy transferred by the wind. They can propagate towards long distances beyond the storm area. The theoretical wave energy potential is estimated to be 32000 TWh per year (Mørk et al., 2010), sufficient to meet the world energy demand of about 22,848 TWh/year reached in 2019 (IEA, 2021). A key factor of wave energy is the predictability and the density distribution, which is about 2-3 kW/m², much higher compared to the solar or wind energy density, in order 0.17 kW/m² and 0.5 kW/m² (Shi et al., 2024). Despite a lot of research having been conducted on those devices, they have still not seen a convergence towards one type of design to harvest wave energy.

Ocean Thermal Energy Conversion (OTEC) harnesses temperature differences between the warm surface water and the cold deep water (between 800 and 1000 m depth) of the ocean to produce electricity. Warm seawater generates vapor, acting as a working fluid for driving a turbine. Cold seawater is used to condense the vapor. OTEC plants are mainly divided into three categories, depending on the fluid used to drive the turbine: open cycle

(sea water), closed cycle (ammonia, chlorofluorocarbon, propane) and hybrid cycle (combination of open and closed cycle) (Abbas et al., 2023).

The salinity gradient is the difference of salt concentrations, especially occurring while mixing freshwater and seawater. The mix occurs where rivers flow into the salty ocean and releases large amounts of energy. This energy can be harvested using pressure retarded osmosis (PRO) to produce electricity (Skilhagen, 2010). Recently, the technical potential for power generation was calculated as 1650 TWh per year (Lewis et al., 2011).

2.2.6 Wind Energy

Wind energy is a widely utilized renewable energy source worldwide, produced by capturing the wind's kinetic energy through a turbine and transforming it into mechanical torque to drive the generator and produce electricity. The devices used to harvest the wind energy are mainly classified considering the axis on which the turbine is mounted: vertical axis wind turbines (VAWTs) and horizontal axis wind turbines (HAWTs).

HAWTs have seen significant development due to their ability to operate at higher level above the surface, where wind conditions are more intense. However, their large size presents a major disadvantage, particularly during the installation phase. VAWTs can harness wind from any direction without the need of gears and controls. However, they operate with weaker and more turbulent ground wind and are notorious for poor reliability, as the lift forces reverse direction with each revolution. One critical aspect of comparison is the conversion efficiency, where HAWTSs reach up to 50% compared to approximately 40% for VAWTs (Mansouri et al., 2023).

Progresses in aerodynamics, structural dynamics, optimization and control strategy, yield to more efficient wind turbine. The annual energy production has risen significantly, such as overall dimensions. In recent years, there has been a shift towards using offshore sites due to better wind conditions, greater available space, and reduced environmental impact. Those are mainly divided into fixed and floating structures (Pires et al., 2022). The combined exploitation of wave and offshore wind energies is a very recent research topic, in order to reduce costs and enhance the energy production (Pérez-Collazo et al., 2015).

2.3 WAVE ENERGY CONVERTERS

Oceans covers up to 70% of the Earth's surface. Wind blows across the sea surface, transferring its energy due to friction among the two fluids and generating ocean waves. A wave is characterized by its height and period, which depend on the intensity and duration of the wind that produces it. Another parameter affecting the shape of waves is the length of water over that wind blows without barriers, known as fetch. The waves formed at the site where the wind blows are known as wind waves. The resulting waves propagate over long distances away. No longer influenced by the wind's forcing, the wave height decreases, and the period become longer. These waves are referred to as swell. The wave power Ψ per unit crest width in deep water is given by Equation (1). It depends on the water density ρ, the gravity acceleration *g*, the significant height H_s and peak wave period T_p of the sea state taken into account.

$$\Psi = \frac{\rho g^2}{64\,\pi} H_s^2\, T_p \qquad \textbf{(1)}$$

Wave energy is classified as an emerging renewable source. The devices used to harvest this natural source are known as Wave Energy Converters (WECs). They are classified upon their working principle, and mainly divided into three categories: Oscillating Bodies (OBs), Overtopping Devices (OTDs) and Oscillating Water Columns (OWCs) (Falcão, 2010).

2.3.1 Oscillating Bodies

Energy generation occurs through the movement of the structure caused by passing waves. These devices can be floating or submerged bodies, consisting of moving structures that generate energy through an oscillatory motion driven by pressure load variations. The main movements are heave and pitch. Maximum energy extraction is achieved when the system reaches resonance conditions with the incident waves. The design of a WEC must be optimized to ensure the system oscillates within the dominant wave frequency range, maximizing motion amplitudes and increasing power generation (Shadman et al., 2018).

In Figure 2 are shown three OBs concept. From left to right, the first and second device are known as Wave Activated Body (WAB), respectively floating and submerged OBs. The third represents the class of Point Absorber (PA), consisting of a buoy equipped with internal mechanisms capable of converting the wave-induced motion into electrical energy.

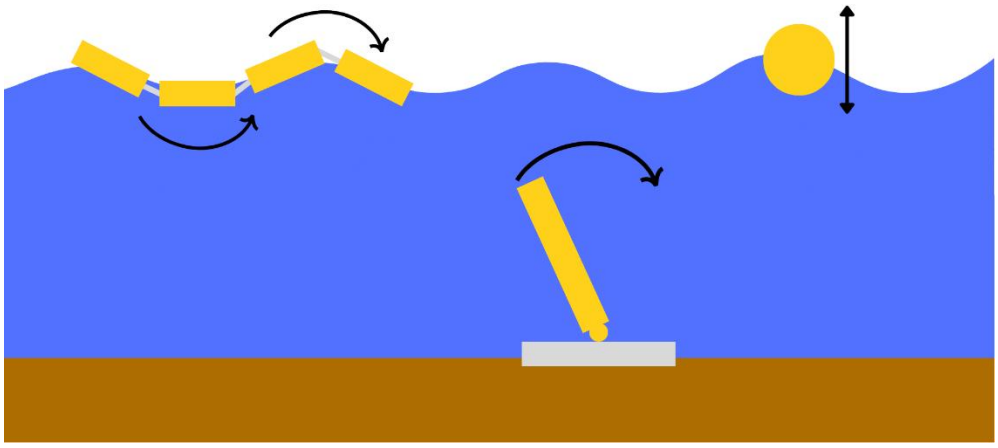

Figure 2 - Oscillating Bodies

One of the most well-known OB is the Pelamis P1 WEC, installed in Portugal in 2008. The system is a semi-submerged snake-like offshore device. It consists of four cylinders, each with a diameter of 3.5 meters, connected in series, forming a total length of 120 meters. Rated at 750 kW and weighted 700 tonnes, it was the first commercial-scale wave energy converter deployed (Thomson et al., 2019). Findings from Pelamis P1 led to the development of its second-generation device, Pelamis P2 WEC (Figure 3), characterized by five cylinders with a diameter of 4 meters, a total length of 180 meters and approximately 1350 tonnes.

Figure 3 - Pelamis P2-001 WEC *(source: Pelamis Wave Power)*

On the other hand, CorPower Ocean's WEC (Figure 4) belongs to the point-absorber category. The energy production is made using a mechanical direct drive PTO inside the buoy. Rated at 300-350 kW, with a buoy height of 18 meters and diameter about 9 meters, weighted 70 tonnes. Currently, it is the only point absorber produced on a commercial scale.

Figure 4 - CorPower WEC *(source: CorPower Ocean)*

2.3.2 Overtopping Devices

Overtopping devices (OTDs) harness wave energy from overtop water waves hitting the structure and conducted over a ramp into an elevated reservoir. The accumulated water is then released to flow through a low-head hydraulic turbine, producing electricity (Figure 5). The first offshore OTD prototype fully installed was the Wave Dragon in Denmark, 2003. It is also the first WEC producing electricity and connected to the electrical grid. It consisted of 57x27 meters wide, two curved ramps and 237 tonnes heavy, equipped with two hydro turbines (Kofoed et al., 2006). In April 2006, a modified prototype was tested at a site with more energetic wave conditions. It was redeployed in 2009 with a 20 kW capacity, but testing ceased in March 2010 due to drifting ice conditions. The prototype was scrapped in 2011. However, due to the development of offshore wind energy, the Danish government redirected funds initially allocated to the project.

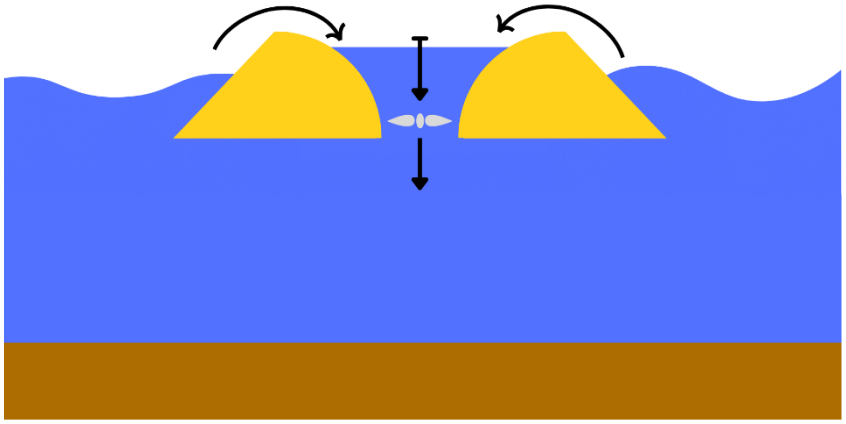

Figure 5 - Overtopping Device

Most of the research has been focused on considering the integration of OTDs into fixed onshore structures, such as breakwaters, in order to reduce overall costs. The Seawave Slot-Cone Generator concept of OTD embedded into a breakwater, includes three reservoirs placed on the top of each other. Through an experimental campaign, quite design tools have been obtained (Buccino et al., 2015). The first full scale prototype of OTD embedded in a breakwater has been installed in the port of Naples. It consists of a ramp followed by a unique reservoir, linked with the turbine. The prototype is composed of two different cross-sections, with different reservoir height, in order to investigate on one side, the most frequent waves, on the other the highest (Palma et al., 2020).

Figure 6 - OTD WEC in the port of Naples *(Palma et al., 2020)*

2.3.3 Oscillating Water Column

The Oscillating Water Column (OWC) WEC harvests the wave energy through the movement of a water column inside the device, driven by the wave motion through an opening located below the mean water level. The vertical displacement of the water column generates a compression (and decompression) of the air pocket located above the surface level, providing an alternating airflow through an opening at the top of the device. The airflow passes through a self-rectifying turbine generating electricity (Figure 7). The turbine needs to be able to rotate in the same direction despite the inlet or outlet airflow. OWCs are the most promising technology among wave energy converters, in terms of reliability and energy production (Babarit, 2015). Absence of moving parts into water, simple and solid infrastructure, easy maintenance and adaptation are the main advantages. They can be deployed both onshore and offshore, floating and fixed, also embedded into existing structures.

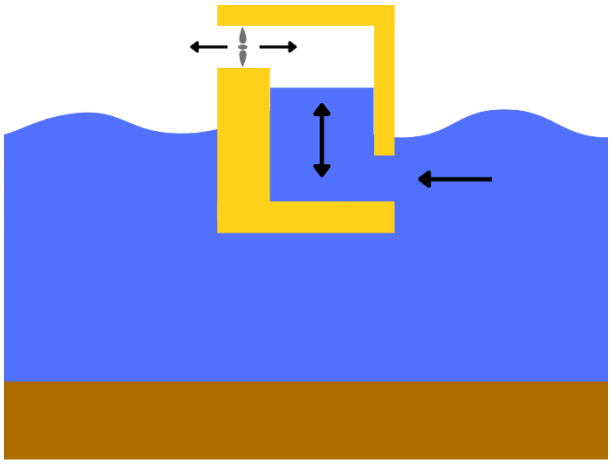

Figure 7 - Oscillating Water Column

Despite quite devices have been proposed, only a few prototypes have been deployed. Onshore devices require simpler installation and maintenance, although facing lower wave energy despite offshore sites. This condition may be overcome due to diffraction conditions in front of a vertical wall, such as port dams, doubling the incident wave height. Prototypes of fixed onshore OWC were built worldwide. In Sakata harbour wall (Japan, 1990) was installed a five chambered OWC about 20 meters long, equipped with two Wells turbine, rated at 60 kW (Vicinanza et al., 2019). Pico power plant, built

in Azores (Portugal, 1999), consists of a 12x12 meter chamber, equipped with a horizontal-axis Wells turbine rated at 400 kW (Falcao et al., 2020). The plant had been running for 1700 hours, the mean electrical power was measured to be 28kW, the efficiency of Wells turbine around 31% (Pecher et al., 2013). LIMPET plant was installed on the Scottish island of Islay (UK, 2000), provided of two Wells turbine each rated at 250 kW, giving the device a 500 kW maximum power output (Heath, 2012).

First OWC deployed for commercial purpose is the breakwater at the port of Mutriku (Spain, 2011). Composed by 16 chambers, each equipped with 18.5 kW Wells turbine (standing in vertical position despite other devices), the Mutriku plant has a total capacity of 296 kW. A monitoring campaign was conducted from January 2014 to October 2016. To evaluate the plant's performance, the capacity factor was introduced, defined as the ratio between the annual energy produced and the theoretical maximum energy output. Based on data collected from 14 turbines, an average annual production of 246 MWh/year was recorded (with an average of ten working turbines). The annual capacity factor was approximately 0.11, although it exhibited significant seasonal variability, reaching 0.22 during the winter months and dropping to 0.03 between July and August (Ibarra-Berastegi et al., 2018).

A new concept of fixed OWC was introduced by Boccoti (2003), known as U-OWC or REWEC3. In contrast to the classical OWC configuration, a vertical wall is placed in front of seaside opening determining a small vertical duct connecting the water column to the open wave field. Such a technological solution accommodates the resonance occurring between the incident waves and the oscillating water column. Several theoretical and also experimental analyses on a small-scale field have been conducted (Boccotti, 2007; Boccotti et al., 2007). The first full-scale U-OWC was built in the port of Civitavecchia in Rome (Italy, 2016). The plant is composed by 17 REWEC3 caissons, 124 independent chambers, each designed to host a turbine rated at 18-20 kW, reaching a potential installed power of 2.2-2.5 MW (Arena et al., 2017).

Offshore sites offer higher wave energy levels. Floating OWC devices have been developed in Japan since 1970, belonging to Yoshio Masuda. The Kaimei barge was deployed at the western cost of Japan in 1978. The barge was 60 meters length, 12 meters wide, equipped with 13 OWC chambers

with a capacity of 125 kW. The Mighty Wale project was developed by the Japan Marine Science and Technology Center and deployed in Gokasho Bay (Japan, 1998). The device was made by three OWC chambers, encompassing a floater of 50 meters length and 30 meters width. Embodying three Wells turbines, two of them with a rated power of 30 kW and the third one with of 50 kW. The device reached 15% as maximum conversion efficiency (Wu et al., 2018). In order to enhance the wave energy production, the Backward Bent-Duct Buoy (BBDB) concept was introduced, based on L-shaped duct with the opening back facing the wave propagation. The first 1:4 scale prototype of BBDB was deployed in Galway (Ireland, 2007), called OE Buoy. Monitoring campaign over three years has demonstrated the conversion efficiency about 30%, demonstrating the reliability and survivability of those floating devices in ocean environment (O'Sullivan et al., 2011). The Spar-Buoy OWC consists of a spar-type offshore structure provided with an inner OWC chamber. The relative motion between the surrounding water and the device generates and oscillating airflow within the air chamber. An experimental campaign was carried out for a 1:32nd-scale model of the Spar-buy OWC at the COAST laboratory ocean basin in Plymouth (UK) (Giorgi et al., 2020).

Despite the relevant number of concepts and prototypes, there has not been reached a convergence towards one type of floating OWC, since none has achieved technologic and economic viability.

CHAPTER 3

Analytical Modelling for OWC

The potential flow theory is widely used for the preliminary analysis of wave energy converters. The boundary value problem and the eigenfunction expansion matching method allows deriving an analytical representation of the velocity potential associated with the fluid region under consideration, with unknowns determined through the matching technique. By neglecting nonlinear effects and applying the principle of superposition, the problem can be separated into the diffraction and radiation wave fields.

This chapter presents a semi-analytical treatment of a vertical cylinder equipped with an internal chamber, based on potential flow theory. It is followed by the modeling of the Power Take-Off (PTO) system and concludes with the introduction of the concept of Capture Width (CW).

3 ANALYTICAL MODELLING FOR CIRCULAR OWC

Development and design of a wave energy converter pass through analytical, numerical and experimental investigations.

Analytical models are used to commonly investigate the wave-structure interaction problem within the framework of linearized wave theory (Airy theory). The linearized theory concerns those problem where the wave amplitude is relatively small compared to the wavelength. Wave field can be decoupled into three main parts: incident, diffracted and radiated wave field. The fluid is assumed to be inviscid and incompressible. Moreover, the assumption of irrotational motion is taken into account, so that the particle paths are closed form, by assuming steady flow conditions. In this context, a velocity potential function can be used to describe the wave field. Main limitations of analytical methods stand upon neglecting the real fluid effects, such as viscosity and turbulence. This leads to power production overestimations. However, they are strongly recommended at the early stages of design, providing important insights and information about the overall performances, in relatively quick time.

In order to better understand the behaviour of wave energy converters, nonlinear models have to be considered. Stokes theory up to third order, such as Cnoidal theory are of acceptable accuracy almost everywhere within the range of validity of each theory, but very high-order expansions are required to get really accurate results (Penalba et al., 2017). Numerical CFD and SPH simulations implement nonlinear models, both solving the Navier-Stokes equations, but differing by the domain discretization method (mesh based against array of particles). Reynold decomposition of fluid velocity is necessary to investigate turbulent flows in CFD simulations. Therefore, Navier-Stokes equations become Reynolds-Average Navier-Stokes (RANS) equations, composed by the continuity equation, the equation of motion and conservation of energy, and cannot be solved analytically. RANS method is widely used, despite large eddy simulation (LES) and direct numerical simulation (DNS), requiring higher computational efforts.

Small-scale and large-scale field tests are required to predict the system stress and dynamic. However, some aspects such as scaled air compressibility have still not been properly addressed, in order to better investigate PTO performances. Moreover, running computational tests

requires huge amount of computational capacity and time, such as the investments necessary to carry out experimental activities.

3.1 LINEARIZED WAVE THEORY

Potential flow theory stands upon assuming inviscid and incompressible fluid properties. Moreover, considering an irrotational motion allows to describe the kinematic conditions by introducing a velocity potential function $\Phi(x,y,z,t)$. The velocity potential requires to be consistent with the fundamental equations of conservation of mass (Laplace equation), kinematic condition at the air-water surface, dynamic condition of pressure continuity (Bernoulli equation), impermeability of the seabed at the depth $z = -d$.

$$\nabla^2\Phi(x,y,z,t) = 0 \tag{2}$$

$$\frac{\partial\eta}{\partial t} + \frac{\partial\Phi}{\partial x}\frac{\partial\eta}{\partial x} + \frac{\partial\Phi}{\partial y}\frac{\partial\eta}{\partial y} = \frac{\partial\Phi}{\partial z} \quad on \;\; z = \eta(x,y,t) \tag{3}$$

$$p + \rho g z + \frac{\rho}{2}\left[\left(\frac{\partial\Phi}{\partial x}\right)^2 + \left(\frac{\partial\Phi}{\partial y}\right)^2 + \left(\frac{\partial\Phi}{\partial z}\right)^2\right] + \rho\frac{\partial\Phi}{\partial t} = 0 \quad on \;\; z = \eta(x,y,t) \tag{4}$$

$$\left(\frac{\partial\Phi}{\partial z}\right)_{z=-d} = 0 \tag{5}$$

The system of equations depends on the surface elevation function $\eta(x,y,t)$; the water density ρ and the fluid pressure p. On the basis of linearized wave theory, assuming a small wave amplitude compared to the wavelength, the non-linear terms of the kinematic and dynamic equation are neglected.

$$\frac{\partial\eta}{\partial t} = \frac{\partial\Phi}{\partial z} \quad on \;\; z = 0 \tag{6}$$

$$g\eta + \frac{\partial\Phi}{\partial t} = 0 \quad on \;\; z = 0 \tag{7}$$

It is possible to merge the kinematic and dynamic equations by differentiating equation (7) with respect to the time *t* and using the equation (6). This process gets to the linearized free-surface condition (time dependent), equation (8).

$$\frac{\partial^2 \Phi}{\partial t^2} + g\frac{\partial \Phi}{\partial z} = 0 \quad on \quad z = 0 \tag{8}$$

3.1.1 Linearized system of equations

Time dependence is removed by considering a time-harmonic motion, depending on a fixed angular frequency ω, and the real part $Re\{\}$ of the complex function.

$$\Phi(x, y, z, t) = Re\{\phi(x, y, z)\, e^{-i\omega t}\} \tag{9}$$

$$\eta(x, y, t) = Re\{\eta(x, y)\, e^{-i\omega t}\} \tag{10}$$

The linearized system of equations, related to time-harmonic motion, is recast as

$$\nabla^2 \phi(x, y, z) = 0 \tag{11}$$

$$\frac{\partial \phi}{\partial z} - \frac{\omega^2}{g}\phi = 0 \quad on \quad z = 0 \tag{12}$$

$$\left(\frac{\partial \phi}{\partial z}\right)_{z=-d} = 0 \tag{13}$$

3.2 EIGENFUNCTION EXPANSION FOR CIRCULAR DOMAINS

The eigenfunction expansion method is employed to tackle the wave-structure interaction problem. Specifically, the separation of variables technique is adopted to represent the velocity potential. In this regard, note that a cylindrical coordinate system (r, θ, z) is adopted for mathematical convenience. where r is the radial distance, θ is the azimuth, and z is the height. Therefore, separation of variables leads to the following representation of the velocity potential function:

$$\phi(r,\theta,z) = R(r)\,\Theta(\theta)\,Z(z) \tag{14}$$

Such a representation is utilized in conjunction with the Laplace equation in cylindrical polar coordinates expressed as

$$\frac{1}{r\,R}\,\frac{\partial}{\partial r}\left(r\,\frac{\partial R}{\partial r}\right) + \frac{1}{r^2\,\Theta}\,\frac{\partial^2\Theta}{\partial\theta^2} + \frac{1}{Z}\,\frac{\partial^2 Z}{\partial z^2} = 0 \tag{15}$$

3.2.1 Vertical eigenfunction

By deriving the equation (15) with respect to ***z***, it is seen that the vertical eigenfunction equals to the constant k_n:

$$\frac{1}{Z}\,\frac{\partial^2 Z}{\partial z^2} = -k_n^2 \tag{16}$$

The solution of the differential equation (16) is written as:

$$Z(z) = C_1\cos[k_n(z+d)] + C_2\sin[k_n(z+d)] \tag{17}$$

Applying the seabed boundary condition (13) shows immediately $C_2 = 0$. The resulting eigenvalues k_n are to be determined by applying the surface boundary conditions (12), leading to the following dispersion relation for a free surface:

$$\frac{\omega^2}{g} + k_n\tan(k_n\,d) = 0 \tag{18}$$

The roots of the eigenvalue k_n will expand within $n = [0, 1, 2, \dots, \infty)$. It is worthily to note that these eigenvalues represent the wavenumbers. The wavenumber k_0 represents the progressive waves, while the other correspond to evanescent waves. Note that equation (18) is not valid for domain without a free-surface. For instance, if the surface boundary conditions (12) is replaced by an impermeable boundary condition at the vertical upper limit $(z = -h)$, the wave numbers are directly given by the equation.

$$k_n = \frac{n\pi}{d-h} \tag{19}$$

It is straightforward to prove the orthogonality of vertical eigenfunctions. Indeed, by integrating over the vertical domain, it is seen that.

$$\int_{-d}^{0} \cos[k_n(z+d)]\ \cos[k_m(z+d)]\ \mathrm{d}z = 0 \qquad with\ n \neq m \tag{20}$$

For later convenience, the vertical eigenfunctions are normalized so that

$$\int_{-d}^{0} \frac{\cos^2[k_n(z+d)]}{N_n^2}\ \mathrm{d}z = d \qquad with\ n = m \tag{21}$$

Whereas:

$$N_n^2 = \frac{1}{2}\left[1 + \sin\frac{(2k_n d)}{2k_n d}\right] \qquad with\ n = m \tag{22}$$

Note that in case of domains impermeable upper boundary these equations are still applicable by observing that in the particular case $n = 0$, equation (21) results in an indeterminate form $0/0$. Thus, in such cases, $N_0 = 1$.

Finally, the vertical normalized eigenfunction assumes the following form:

$$Z(z) = C_1 \frac{\cos[k_n(z+d)]}{N_n} \tag{23}$$

3.2.2 Circular eigenfunction

Once the vertical eigenfunction has been determined, it is possible to substitute the results of equation (16) into (15). In order to derive the circular eigenfunction, all the terms are multiplied by r^2, so that:

$$\frac{r}{R}\frac{\partial}{\partial r}\left(r\ \frac{\partial R}{\partial r}\right) + \frac{1}{\Theta}\frac{\partial^2 \Theta}{\partial \theta^2} - r^2 k_n^2 = 0 \tag{24}$$

For deriving the representations of $\Theta(\theta)$ two cases are considered. The first case involves a function defined over the whole circular domain. The second case considers a function defined over a restricted interval $\Delta\theta = \theta_{fin} - \theta_{in} < 2\pi$.

In the first case, following the separation of variable technique, it is seen that the equation governing the Θ dependence must be consistent with the equation

$$\frac{1}{\Theta}\frac{\partial^2\Theta}{\partial\theta^2} = -m^2 \quad \textbf{(25)}$$

The general solution of the differential equation (25) is:

$$\Theta(\theta) = C_3\cos(m\theta) + C_4\sin(m\theta) \quad \textbf{(26)}$$

Dealing with a domain enclosed within $\theta = [0, 2\pi]$, the orthogonality of the functions in θ is used to eliminate terms in $\sin(m\theta)$ (Linton and McIver, 2001). Thus, the circular eigenfunction assumes the following form:

$$\Theta(\theta) = C_3\cos(m\theta) \quad \textbf{(27)}$$

Considering the second case in which the potential pertains to a circular domain $\theta = [\theta_{in}, \theta_{fin}]$, in which $\Delta\theta = \theta_{fin} - \theta_{in} < 2\pi$, equation (24) results in the form

$$\frac{1}{\Theta}\frac{\partial^2\Theta}{\partial\theta^2} = -m^2\beta^2 \quad \textbf{(28)}$$

whose general solution is

$$\Theta(\theta) = C_3\cos[m\beta(\theta - \theta_{in})] + C_4\sin[m\beta(\theta - \theta_{in})] \quad \textbf{(29)}$$

Considering that this solution is employed in conjunction with the boundary conditions referring to the velocity against the limits of the circular domain:

$$\left(\frac{\partial \phi}{\partial \theta}\right)_{\theta=\theta_{in}} = 0 \quad \textbf{(30)}$$

$$\left(\frac{\partial \phi}{\partial \theta}\right)_{\theta=\theta_{fin}} = 0 \quad \textbf{(31)}$$

Applying the boundary condition (30) within the general solution (29), shows immediately that $C_4 = 0$. Using the boundary condition (31) renders β:

$$\beta = \frac{\pi}{\theta_{fin} - \theta_{in}} \quad \textbf{(32)}$$

The circular eigenfunction, referring to domains enclosed within circular domain $\Delta\theta = \theta_{fin} - \theta_{in} < 2\pi$ assumes the following form:

$$\Theta(\theta) = C_3 \cos[m\beta(\theta - \theta_{in})] \quad \textbf{(33)}$$

3.2.3 Radial eigenfunction

Once the vertical and circular eigenfunctions have been defined, using equations (16) and (25), or equation (28), into (15) leads to the equation

$$\frac{r}{R}\frac{\partial}{\partial r}\left(r\,\frac{\partial R}{\partial r}\right) - m^2 - k_n^2 r^2 = 0 \quad \textbf{(34)}$$

Expanding the first term, and multiplying all the terms by the function R, will lead to:

$$r^2\frac{\partial^2 R}{\partial r^2} + r\,\frac{\partial R}{\partial r} - (m^2 - k_n^2 r^2)R = 0 \quad \textbf{(35)}$$

The previous equation is the Bessel differential equation. Its general solution stands upon the Bessel modified functions $I_m(k_n r)$ and $K_m(k_n r)$ of order m and argument $k_n r$:

$$R(r) = C_5\, I_m(k_n r) + C_6\, K_m(k_n r) \quad \textbf{(36)}$$

In Figure 8 are depicted both the Modified Bessel function of order $m = 0, 1, 2$. The Modified Bessel function of the first kind $I_m(k_n r)$ approaches zero for very small values, while describes an asymptotic behaviour occuring $k_n r \to +\infty$. The Modified Bessel function of the second kind $K_m(k_n r)$ shows an opposite behaviour, exhibiting an asymptotic behaviour with small argument values, and moving to zero as $k_n r \to +\infty$. This behavior is reflected in the definition of the velocity potentials, referring to the specific domains.

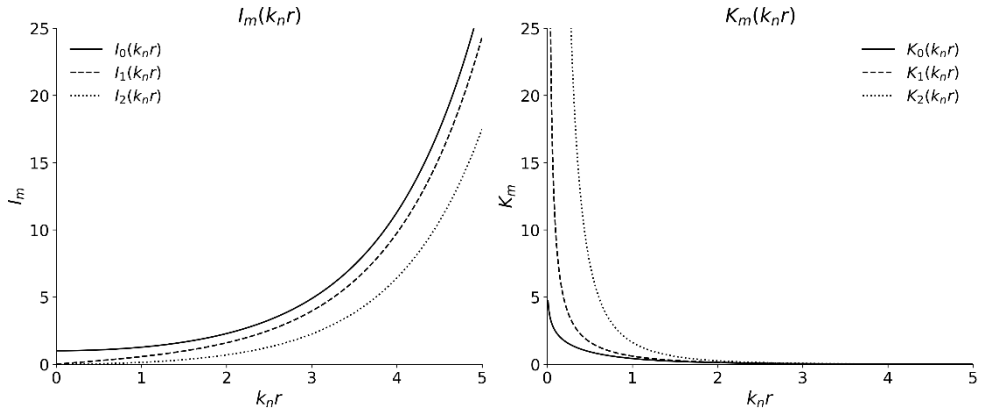

Figure 8 - Bessel Modified Functions

3.2.4 Matching Eigenfunction Method

The eigenfunction matching method is a widely used technique for solving wave-structure interaction problems developed within the linearized potential flow theory. This approach is applicable to problems involving simple geometrical configurations, where the domain can be eventually divided into simple sub-domains. In this context, the velocity potential is derived by using the separation of variables technique and invoking the pertinent boundary conditions. The representation of the velocity potential involves an infinite series of separated eigenfunctions with unknown coefficients. The unknowns are determined via a matching technique, in which the continuity of pressure and of velocity is enforced at the interface between two adjacent domains. In this manner, orthogonality of the eigenfunctions can be exploited for estimating the coefficients as a solution of a linear system of algebraic equations. The eigenfunctions are orthogonal, and can be normalized to be

orthonormal, in order to diagonalize the terms of the resulting coefficient matrix. The infinite series of eigenfunctions of each region is truncated at a certain threshold that ensures the convergence of the results. The application of the technique is given in the next sections, where it is applied in conjunction with the diffraction and radiation problems of the proposed circular OWC device.

3.3 DIFFRACTION AND RADIATION PROBLEM

The use of linearized potential theory allows for the application of the superposition principle. The wave field is decoupled into three main contributions that need to be taken into account: incident waves, diffracted waves and radiated waves. By exploiting linearity, it is possible to separate the resolution of this complex problem into simpler problems, each of them is analyzed individually and later combined. Incident wave field $\phi_I(r,\theta,z)$ is made by the undisturbed incoming waves. The diffracted wave field $\phi_D(r,\theta,z)$ is generated by the interaction between incident waves and the structure, which is supposed fixed. Radiated waves field $\phi_R(r,\theta,z)$ belong to the six body motions of the structure. In this regard, note that by dealing with OWC investigation, also the effect of the wave field associated with the oscillating air pressure inside the device is taken into account and regarded as a radiation source. Therefore,

$$\phi(r,\theta,z) = \phi_I(r,\theta,z) + \phi_D(r,\theta,z) + \sum \phi_R(r,\theta,z) \qquad \textbf{(37)}$$

In order to conduct the hydrodynamics investigation, as depicted in Figure 9, two main problems are considered:

1) Diffraction problem
   The structure is restrained of oscillations, even if it is floating, while being forced simultaneously by the incident wave field and the diffracted wave field.

2) Radiation problem
   There are no incident waves, the water is initially calm and flat. The structure is forced to oscillate due to the motion modes, one degree

of freedom at time. Hydrodynamic loads are referred to added mass and radiation damping coefficients.

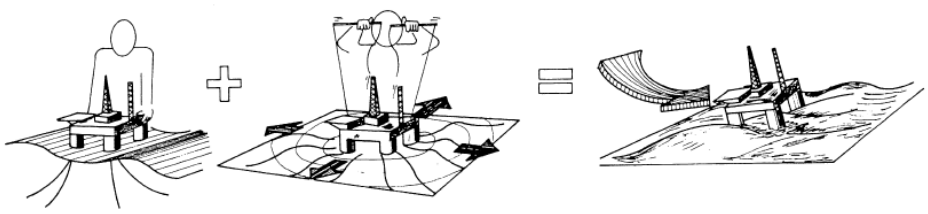

Figure 9 - Superposition of diffraction and radiation *(Faltinsen, 1990)*

3.4 POWER TAKE OFF MODELLING

The OWC devices need to be equipped with a specific Power Take Off (PTO) in order to harvest the wave energy. As widely investigated by Falcão and Henriques (2016), Wells turbine and impulse turbine are the most self-rectifying axial-flow turbines deployed within OWC devices. The main feature is about the same rotational direction despite the airflow, thanks to special guide vanes and others rectifying mechanisms. Both turbines have their pros and cons: the Wells turbine achieves a peak efficiency of 75% (under laboratory conditions), compared to the 50% (almost 60%) efficiency of the impulse turbine. However, despite its better performance, the operating range is narrower.

In order to model the PTO, the free surface of the oscillating water column is commonly assumed as a piston-like flat motion. However, a more realistic approach assumes a spatially uniform air pressure distribution on the free surface. To investigate the behavior of the water column, the volume flow rate parameter $q(t)$ is introduced, depending on the water volume variation despite the time (assuming positive value for upward motion).

$$q(t) = -\frac{dV}{dt} \tag{38}$$

Assuming linear water wave theory, dealing within the uniform air pressure distribution model, it is possible to split the volume flow rate referring to the diffraction and radiation problems:

$$q(t) = q_e(t) + q_r(t) \tag{39}$$

Excitation (or diffraction) volume flow rate $q_e(t)$ refers to the diffraction problem, and depends on incident waves, considering the upper part of the chamber fully opened and neglecting the pressure inside. Radiation volume flow rate $q_r(t)$ belongs just to the air pressure oscillations $p(t)$ inside the closed chamber, while neglecting the incident and diffracted waves.

It is possible to separate the time dependency. Under the assumption of a linear model, the response to a sinusoidal signal is another sinusoidal signal (potentially with a phase difference). This enables the use of frequency-domain analysis, dealing with the complex amplitudes of the quantity involved:

$$q(t);\ q_e(t);\ q_r(t);\ p(t) = Re\{(Q; Q_e; Q_r; P)e^{-i\omega t}\} \tag{40}$$

So that, referring to a circular domain:

$$Q_e = \int_r \int_\theta \frac{\partial \phi_D(r,\theta,0)}{\partial z}\, r\, dr d\theta \tag{41}$$

$$Q_r = \int_r \int_\theta \frac{\partial \phi_R(r,\theta,0)}{\partial z}\, r\, dr d\theta = -(C - iM_{add})\, P \tag{42}$$

The radiation damping C and the added mass M_{add} are represented by the real and imaginary part of the radiate volume flow rate (Lovas et al., 2010; Zheng et al., 2019).

3.4.1 Air chamber thermodynamics

The air compressibility inside the chamber was widely investigated by Falcão et al. (2016). An isentropic process occurs while air flows out. Nevertheless, due to viscous losses through the turbine, entropy increases while air flows in. While temperature oscillations are relatively small and no significant heat

exchanges are showed, air density into the chamber is affected by the pressure variation (Falcão and Henriques, 2014).

In order to investigate the air density inside the chamber, the polytropic relationship between pressure (inside p and outside p_{atm}) and air density (inside ρ_{ch} and outside ρ_{atm}), is taken into account:

$$\frac{p_{atm} + p}{\rho_{ch}^{k}} = \frac{p_{atm}}{\rho_{atm}^{k}} \tag{43}$$

The polytropic coefficient k refers to the average efficiency $\bar{\eta}$ of the turbine. Usually is assumed equals to $k = 1.25$.

$$k = 0.13\,\bar{\eta}^2 + 0.27\bar{\eta} + 1 \tag{44}$$

From equation (43) is derived the form of the air density inside the chamber:

$$\rho_{ch} = \frac{(p_{atm} + p)^{\frac{1}{k}}\,\rho_{atm}}{p_{atm}} \tag{45}$$

Differentiating in respect of time will shows:

$$\frac{\partial \rho_{ch}}{\partial t} = \frac{\rho_{atm}}{k\,(p_{atm} + p)^{\frac{k-1}{k}}\;p_{atm}^{\frac{1}{k}}}\,\frac{\partial p}{\partial t} \tag{46}$$

Equation (46) describes the relationship between the variation in air density within the chamber and the pressure variation, based on the polytropic relation and the air density outside the chamber. It can be assumed that atmospheric pressure is significantly higher than the pressure inside the chamber $(p_{atm} \gg p)$, leading to two important simplifications. The first simplification concerns equation (46):

$$\frac{\partial \rho_{ch}}{\partial t} = \frac{\rho_{atm}}{k\,p_{atm}}\,\frac{\partial p}{\partial t} \tag{47}$$

The second simplification is referred to equation (43), through which we can establish that there is no difference between the air density inside and outside the chamber:

$$\rho_{ch} = \rho_{atm} \tag{48}$$

3.4.2 Air turbine aerodynamics

Air turbines implemented into OWC devices are used to face highly unsteady flows due to the bidirectional air path. The mass flow rate $w(t)$ through the turbine is evaluated such as the variation of air mass into the chamber:

$$w(t) = -\frac{\partial m_{ch}}{\partial t} \tag{49}$$

Expressing the mass of air contained in the chamber as the product of air density ϱ_{ch} and volume V_0 referred to steady conditions, and developing its derivative, we obtain:

$$w(t) = -V_0 \frac{\partial \rho_{ch}}{\partial t} - \rho_{ch} \frac{\partial V_0}{\partial t} \tag{50}$$

By substituting equation (47) into the previous one, and recalling the equality between the air density inside and outside the chamber as represented in equation (48) (resulted from the assumption that atmospheric pressure is higher than the pressure inside the chamber), considering that the time variation of volume represents the volume flow rate $q(t)$, we obtain the air flow through the turbine:

$$w(t) = -V_0 \frac{\rho_{atm}}{k\, p_{atm}} \frac{dp}{dt} + \rho_{atm} q(t) \tag{51}$$

3.4.3 Linearized PTO system

The turbine performance can be investigated through a linear condition between the dimensionless airflow rate Ψ through the turbine and the dimensionless pressure Π:

$$\Psi = \Xi\, \Pi \tag{52}$$

The parameter Ξ refers to the type of turbine ($\Xi = 1$ for the Wells turbine, $\Xi = 0.2$ for the biradial turbine). The pressure and airflow rate in equation (52) have been properly nondimensionalized by considering the rotor diameter of the turbine and the rotational speed:

$$\Psi = \frac{w}{\rho_{atm} \Omega D^3} \tag{53}$$

$$\Pi = \frac{w}{\rho_{atm} \Omega D^3} \tag{54}$$

Substituting the previous formulations into equation (52), in order to define the mass flow rate through the turbine:

$$w = K\, \rho_{atm}\, p \tag{55}$$

Utilizing the mass flow rate definition obtained into equation (51) and (55):

$$-V_0 \frac{\rho_{atm}}{k\, p_{atm}} \frac{dp}{dt} + \rho_{atm} q(t) = C_{PTO}\, \rho_{atm}\, p \tag{56}$$

The parameter C_{PTO} is introduced to represents the main turbine factors:

$$C_{PTO} = \frac{\Xi\, D}{\rho_{atm} \Omega} \tag{57}$$

From the previous equation will follow the linearized PTO equation:

$$q(t) = C_{PTO}\, p + \frac{V_0}{k\, p_{atm}} \frac{dp}{dt} \tag{58}$$

Due to the linearized theory assumption, it is possible to evaluate the PTO in frequency domain. Remembering the discharge superposition in equation (39) and the complex amplitude described in equation (40), according to the radiate flow defined in equation (42), the linearized PTO system in frequency domain is described as follows:

$$P = \frac{Q_e}{[C + C_{PTO} - i(M_{ADD} + M_{PTO})]} \quad \textbf{(59)}$$

In which:

$$M_{PTO} = \frac{\omega\, V_0}{k\, p_{atm}} \quad \textbf{(60)}$$

Once the pressure inside the OWC device is determined, it becomes possible to calculate the time-averaged power available to the PTO.

$$P_{mean} = \frac{1}{T}\int_0^T P(t)\, dt \quad \textbf{(61)}$$

By developing the calculations and using the pressure definition, we derive:

$$P_{mean} = \frac{C_{PTO}}{2}|P|^2 \quad \textbf{(62)}$$

The power available to the turbine, for a single frequency, depends on the PTO characteristics in terms of turbine diameter and rotational speed, as well as the pressure achieved within the chamber. The maximum pressure, in turn, is reached when resonance conditions occur, that is, when the added mass equals the mass of the PTO. Therefore, it is challenging to vary the internal volume of the chamber. As described by Michele et al. (2019) it is possible to define the damping characteristics of the PTO such that the derivative of the average power with respect to C_{PTO} is zero, thereby obtaining the optimal $C_{PTO-OPT}$ value:

$$C_{PTO-OPT} = \sqrt{C^2 + (M_{PTO} + M_{ADD})^2} \quad \textbf{(63)}$$

3.5 CAPTURE WIDTH

Due to the huge number of devices proposed, analyzed and deployed for wave energy conversion, a common value has been introduced in the literature to evaluate the energy performance of a wave energy converter, known as the Capture Width (CW). This parameter expresses the ratio

between the mean power available to the PTO and the power of the incident waves.

$$CW = \frac{P_{mean}}{P_{INC}} \tag{64}$$

The incident wave power is calculated by considering the group celerity C_g and the amplitude of the incident wave A:

$$P_{INC} = \frac{1}{2}\rho g C_g A^2 \tag{65}$$

The group celerity is calculated through the wave period T and the progressive wave number $k_0 = -ik$:

$$C_g = \frac{gT}{4\pi}\tanh(kd)\left[1 + \frac{2kd}{\sinh(2kd)}\right] \tag{66}$$

To compare devices of different sizes, the Capture Width Ratio (CWR) is introduced, dividing the CW by a characteristic length of the device D_k.

$$CWR = \frac{CW}{D_k} \tag{67}$$

CHAPTER 4

Single-chamber circular OWC

Circular Oscillating Water Column devices are typically equipped with a single internal chamber for energy conversion. The competitiveness of such devices depends on their energy productivity. Optimization can be achieved by analyzing the contribution of individual geometric parameters.

This chapter presents a semi-analytical solution for a circular OWC, equipped with a single inner chamber. All main geometric parameters are investigated, with particular attention given to analyzing the angular width of the internal chamber.

4 SINGLE-CHAMBER CIRCULAR OWC

4.1 General Overview

Circular OWC are commonly used referring to an inner chamber spanning the whole sector. Although extensive research has been conducted on circular oscillating water column devices, no convergence has been reached regarding a single optimal design. Evans and Porter (1995) analyzed the hydrodynamics of a 2D thin vertical OWC under the framework of linearized potential flow theory. Martins-Rivas and Mei (2009) explored a circular OWC installed at the tip of a thin breakwater. Their analytical solution demonstrated that the device's energy absorption remains unaffected by the incidence angle of incoming waves. Lovas et al. (2010) extended analytical theories to evaluate a large circular OWC placed at the tip of a coastal corner with two specific geometries: convex and concave right-angle corners. Using the eigenfunction matching method to solve the radiation and diffraction problems, they showed the influence of key geometrical parameters. To enhance wave energy extraction, Deng et al. (2014) developed an analytical model for a circular bottom-mounted OWC featuring a V-shaped channel at its opening. Michele et al. (2019) studied a circular OWC with an internal cylinder and an external skirt, highlighting their significant impact on the device's overall performance. Zheng et al. (2020) examined the effects of the chamber opening's size and position. While previous studies on circular OWCs have considered designs with inner chambers spanning the entire sector, Spanò et al. (2024) conducted parametric investigations showing that reducing the angular width of the inner chamber is a key strategy for improving energy performance.

In order to evaluate the features of circular OWC, dealing with geometrical parameters, an analytical solution has been developed.

4.2 Analytical Model

4.2.1 Geometrical configuration

The circular OWC embedded within a vertical cylindrical floating structure is showed in Figure 10. It is described throughout a cylindrical coordinate system $O_{r\theta z}$, with its origin located at the still water level at the center of the cylinder and the vertical axis oriented upwards. The system operates in a constant water depth d. The geometry of the cylinder is defined by an

external radius R_3 and a total height h_3. The single OWC chamber, entirely enclosed within the structure, has an angular width $\Delta\theta$, symmetrically aligned with the x-axis, and spans a radial distance $\Delta r = R_2 - R_1$. The inner chamber is connected to the open wave field through a vertical opening of angular width $\Delta\theta$ and height $h_l = h_2 - h_1$, ensuring that the opening remains fully submerged.

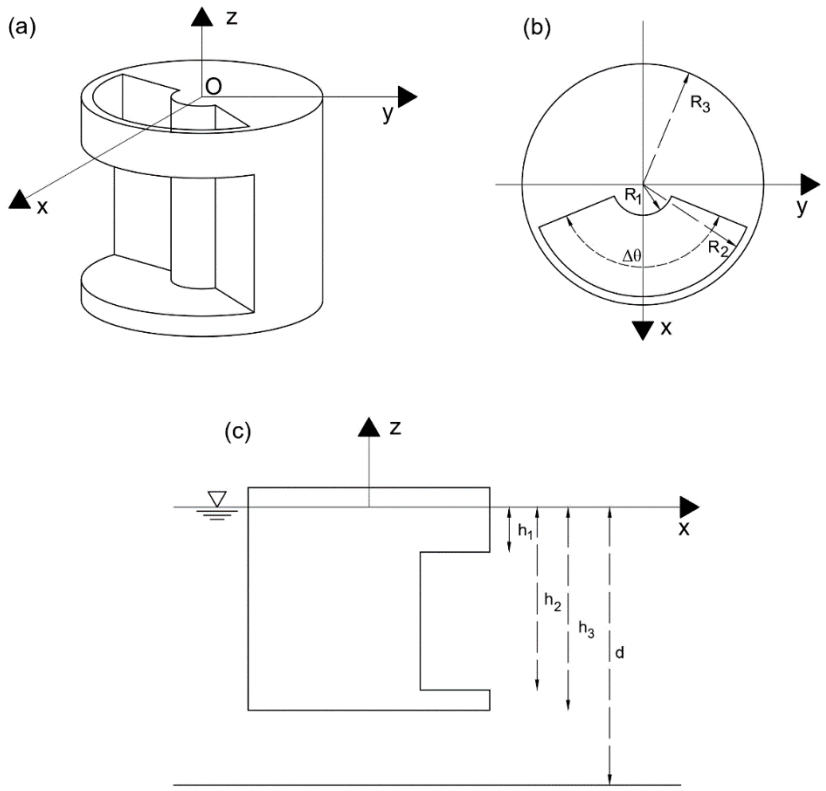

Figure 10 - Geometrical configuration of the OWC: (a) three dimensional views; (b) top view; (c) side view

4.2.2 Boundary value problem

In order to apply the linearized wave theory and define the velocity potential, the domain is divided into four sub-domains:

$$\Omega_1(r,\theta,z) = \{\, \mathrm{r} \in [R_3;\ +\infty);\ z \in [-d;\ 0];\ \ \theta \in [0; 2\pi]\}$$

$$\Omega_2(r,\theta,z) = \{\mathrm{r} \in [0;\ R_3]\ ;\ z \in [-d;\ -h_3];\ \ \theta \in [0; 2\pi]\}$$

$$\Omega_3(r,\theta,z) = \left\{\mathrm{r} \in [\mathrm{R}_1;\ R_2]\ ;\ z \in [-h_2;\ 0];\ \ \theta \in \left[-\frac{\Delta\theta}{2}\ ;\frac{\Delta\theta}{2}\right]\right\}$$

$$\Omega_4(r,\theta,z) = \left\{\mathrm{r} \in [\mathrm{R}_2;\ R_3]\ ;\ z \in [-h_2; -h_1];\ \ \theta \in \left[-\frac{\Delta\theta}{2}\ ;\frac{\Delta\theta}{2}\right]\right\}$$

The velocity potential $\phi_{\lambda,i}$ for each i-th sub-domain is calculated by satisfying the boundary value system of equations, regarding both diffracted ($\lambda = D$) and radiated ($\lambda = R$) problems:

$$\nabla^2 \phi_{\lambda,i}\,(r,\theta,z) = 0 \qquad \textbf{(68)}$$

$$\frac{\partial \phi_{\lambda,1}}{\partial z} - \frac{\omega^2}{g}\,\phi_{\lambda,1} = 0 \quad in\ z = 0 \qquad \textbf{(69)}$$

$$\frac{\partial \phi_{\lambda,3}}{\partial z} - \frac{\omega^2}{g}\,\phi_{\lambda,3} = \begin{cases} 0 & z = 0, \lambda = D \\ \dfrac{i\omega P}{\rho g} & z = 0, \lambda = R \end{cases} \qquad \textbf{(70)}$$

$$\frac{\partial \phi_{\lambda,i}}{\partial \boldsymbol{n}} = 0 \quad on\ the\ cylinder\ boundary\ and\ seabed \qquad \textbf{(71)}$$

$$\lim_{kr \to \infty} \sqrt{r}\left(\frac{\partial \phi_{\lambda,1}}{\partial z} - ik\phi_{\lambda,1}\right) = 0 \qquad \textbf{(72)}$$

Into the kinematic equations (71), $\boldsymbol{n}$ represents the unit vector normal to the solid boundary of the problem (both the device and the seabed). The air pressure inside the chamber is reported as P, water density with ρ. The

equation (72) asses the boundness of diffracted and radiated waves propagating away from the structures (see §1.3.1 in Linton and McIver, 2001).

4.2.3 Velocity potentials

Considering the separation of variables techniques, eigenfunction expansion method, and equations (68)-(72), the velocity potentials assumes the following form:

$$\phi_{\lambda,1}(r,\theta,z) = \kappa \sum_{m=0}^{\infty}\sum_{n=0}^{\infty} \alpha_{mn}^{(\lambda,1)} F_{mn}^{(1)}\ cos(m\theta)\,\chi_n^{(1)} + \phi_I \delta_{\lambda D} \qquad \textbf{(73)}$$

$$\phi_{\lambda,2}(r,\theta,z) = \kappa \sum_{m=0}^{\infty}\sum_{n=0}^{\infty} \alpha_{mn}^{(\lambda,2)} F_{mn}^{(2)}\ cos(m\theta)\,\chi_n^{(2)} \qquad \textbf{(74)}$$

$$\phi_{\lambda,3}(r,\theta,z) = \kappa \sum_{m=0}^{\infty}\sum_{n=0}^{\infty} \alpha_{mn}^{(\lambda,3)} F_{mn}^{(3)}\ cos\left[m\beta\left(\theta+\frac{\Delta\theta}{2}\right)\right]\chi_n^{(3)} - \delta_{\lambda R} \qquad \textbf{(75)}$$

$$\phi_{\lambda,4}(r,\theta,z) = \kappa \sum_{m=0}^{\infty}\sum_{n=0}^{\infty} \left[\alpha_{mn}^{(\lambda,4A)} F_{mn}^{(4A)} + \alpha_{mn}^{(\lambda,4B)} F_{mn}^{(4B)}\right] cos\left[m\beta\left(\theta+\frac{\Delta\theta}{2}\right)\right]\chi_n^{(4)} \qquad \textbf{(76)}$$

Where $\alpha_{mn}^{(\lambda,1)}, \alpha_{mn}^{(\lambda,2)}, \alpha_{mn}^{(\lambda,3)}, \alpha_{mn}^{(\lambda,4A)}, \alpha_{mn}^{(\lambda,4B)}$ are the unknown terms to be determined. The constant $\kappa = \left(-\frac{igA}{\omega}\delta_{\lambda D} - \frac{iP}{\rho\omega}\delta_{\lambda R}\right)$ refers to the diffracted or radiated problems, depending on the Kronecker delta function $\delta_{\lambda D} = 1$ whenever $\lambda = D$ otherwise $\delta_{\lambda D} = 0$ (same assumptions for $\delta_{\lambda R}$). The vertical eigenfunctions are written as $\chi_n^{(1)}, \chi_n^{(2)}, \chi_n^{(3)}, \chi_n^{(4)}$.Bessel functions are normalized and reported as $F_{mn}^{(1)}, F_{mn}^{(2)}, F_{mn}^{(3)}, F_{mn}^{(4A)}, F_{mn}^{(4B)}$ such as:

$$F_{mn}^{(1)} = \frac{K_m\left(k_n^{(1)} r\right)}{K_m\left(k_n^{(1)} R_3\right)} \qquad \textbf{(77)}$$

$$F_{mn}^{(2)}(r) = \begin{cases} \left(\frac{r}{R_3}\right)^m, n = 0 \\ \frac{I_m\left(k_n^{(2)} r\right)}{I_m\left(k_n^{(2)} R_3\right)}, n > 0 \end{cases} \quad (78)$$

$$F_{mn}^{(3)}(r) = \left[\frac{I_{m\beta}\left(k_n^{(3)} r\right)}{I_{m\beta}\left(k_n^{(3)} R_2\right)} - \frac{K_{m\beta}\left(k_n^{(3)} r\right) I'_{m\beta}\left(k_n^{(3)} R_1\right)}{I_{m\beta}\left(k_n^{(3)} R_2\right) K'_{m\beta}\left(k_n^{(3)} R_1\right)}\right] \quad (79)$$

$$F_{mn}^{(4,A)}(r) = \begin{cases} \left(\frac{r}{R_3}\right)^m & n = 0 \\ \frac{I_{m\beta}\left(k_n^{(4)} r\right)}{I_{m\beta}\left(k_n^{(4)} R_3\right)} & n > 0 \end{cases} \quad (80)$$

$$F_{mn}^{(4,B)}(r) = \begin{cases} ln\left(\frac{r}{R_2}\right) + 1 & n = m = 0 \\ \left(\frac{r}{R_2}\right)^{-m} & n = 0;\ m > 0 \\ \frac{K_{m\beta}\left(k_n^{(4)} r\right)}{K_{m\beta}\left(k_n^{(4)} R_2\right)} & n > 0; m > 0 \end{cases} \quad (81)$$

Modified Bessel function of the first kind $I_m(k_n r)$ and second kind $K_m(k_n r)$, and their derivates are taken into account, depending on the wavenumber $k_n^{(i)}$ evaluated for each i-th subdomain throughout the linearized free surface condition reported into equations (69)-(70) and applying equation (71) vertically.

$$k_n^{(1)}\, tan\left(k_n^{(1)} d\right) = -\frac{\omega^2}{g} \quad (82)$$

$$k_n^{(2)} = \frac{n\pi}{d - h_3} \quad (83)$$

$$k_n^{(3)}\, tan\left(k_n^{(3)} h_2\right) = -\frac{\omega^2}{g} \quad (84)$$

$$k_n^{(4)} = \frac{n\pi}{h_2 - h_1} \tag{85}$$

Once evaluated the wavenumbers, it is possible to calculate the vertical eigenfunctions:

$$\chi_n^{(1)}(z) = cos\left[k_n^{(1)}(z+d)\right]\left\{\frac{1}{2}\left[1 + \frac{sin\left(2k_n^{(1)}d\right)}{2k_n^{(1)}d}\right]\right\}^{-0.5} \tag{86}$$

$$\chi_n^{(2)}(z) = \begin{cases} cos\left[k_0^{(2)}\,(z+d)\right] & for\ n = 0 \\ \left(1/2\right)^{-0.5}\ cos\left[k_n^{(2)}\,(z+d)\right] & for\ n > 0 \end{cases} \tag{87}$$

$$\chi_n^{(3)}(z) = cos\left[k_n^{(3)}(z+h_2)\right]\left\{\frac{1}{2}\left[1 + \frac{sin\left(2k_n^{(3)}h_2\right)}{2k_n^{(3)}h_2}\right]\right\}^{-0.5} \tag{88}$$

$$\chi_n^{(4)}(z) = \begin{cases} cos\left[k_0^{(4)}\,(z+h_2)\right] & for\ n = 0 \\ \left(1/2\right)^{-0.5}\ cos\left[k_n^{(4)}\,(z+h_2)\right] & for\ n > 0 \end{cases} \tag{89}$$

4.2.4 Computation of the unknown terms

The unknown terms $\alpha_{mn}^{(\lambda,1)}, \alpha_{mn}^{(\lambda,2)}, \alpha_{mn}^{(\lambda,3)}, \alpha_{mn}^{(\lambda,4A)}, \alpha_{mn}^{(\lambda,4B)}$ of the velocity potentials, are evaluated through the eigenfunction matching method. By enforcing the continuity of pressure and velocity among adjacent domains, will follows the system to be solved:

$$\left(\phi_{\lambda,1}\right)_{r=R_3} = \left(\phi_{\lambda,2}\right)_{r=R_3} \quad z \in [-d;\ -h_3];\ \ \theta \in [0; 2\pi] \tag{90}$$

$$\left(\phi_{\lambda,1}\right)_{r=R_3} = \left(\phi_{\lambda,4}\right)_{r=R_3} \quad z \in [-h_2;\ -h_1];\ \ \theta \in \left[-\frac{\Delta\theta}{2}; \frac{\Delta\theta}{2}\right] \tag{91}$$

$$\left(\phi_{\lambda,3}\right)_{r=R_2} = \left(\phi_{\lambda,4}\right)_{r=R_2} \quad z \in [-h_2;\ -h_1];\ \ \theta \in \left[-\frac{\Delta\theta}{2}; \frac{\Delta\theta}{2}\right] \tag{92}$$

$$\left(\frac{\partial \phi_{\lambda,1}}{\partial r}\right)_{r=R_3} = \begin{cases} \left(\frac{d\partial \phi_{\lambda,2}}{\partial dr}\right)_{r=R_3} & z \in [-d;\ -h_3];\ \ \theta \in [0; 2\pi] \\ \left(\frac{\partial \phi_{\lambda,4}}{\partial r}\right)_{r=R_3} & z \in [-h_2; -h_1\ ];\ \ \theta \in \left[-\frac{\Delta\theta}{2};\ \frac{\Delta\theta}{2}\right] \\ 0 & z \in [-h_1; 0\ ];\ \ \theta \in [0; 2\pi] \end{cases} \quad \textbf{(93)}$$

$$\left(\frac{\partial \phi_{\lambda,3}}{\partial r}\right)_{r=R_2} = \begin{cases} \left(\frac{\partial \phi_{\lambda,4}}{\partial r}\right)_{r=R_2} & z \in [-h_2;\ -h_1];\ \ \theta \in \left[-\frac{\Delta\theta}{2};\ \frac{\Delta\theta}{2}\right] \\ 0 & z \in [-h_1;\ 0];\ \ \theta \in \left[-\frac{\Delta\theta}{2};\ \frac{\Delta\theta}{2}\right] \end{cases} \quad \textbf{(94)}$$

4.3 RESULTS

The design of an OWC device must ensure its operation at frequencies corresponding to the highest energy bandwidth, based on the site selected for the deployment. Each geometric parameter influences the device's energy capabilities, some more significantly than others. By employing the analytical model, different parametric investigations are conducted to examine the effects of individual components. The device's performance will be evaluated through the excitation flow rate (in absolute value), radiation damping, and added mass, all appropriately non-dimensionalized as made by Lovas et al. (2010).

$$\overline{Q_e} = \frac{\sqrt{g/d}}{A\ d\ g}\ Q_e \quad \textbf{(95)}$$

$$(\bar{C}, \overline{M_{ADD}}, \overline{C_{PTO}}, \overline{M_{PTO}}) = \frac{\rho\sqrt{g/d}}{d}\ (C, M_{ADD}, C_{PTO}, M_{PTO}) \quad \textbf{(96)}$$

Furthermore, the capture width ratio (CWR) is taken into account, referring to the characteristic dimension as the outer diameter $D_K = 2R_3$:

$$CWR = \frac{P_{mean}}{2R_3\ P_{INC}} \quad \textbf{(97)}$$

4.3.1 Validation of the model

The velocity potentials are formulated as a summation of eigenfunctions. A convergence study was conducted to investigate the minimum number of terms required for the vertical eigenfunctions. For this purpose, a specific geometry was fixed, with its values reported in the following table, properly scaled on the seabed value.

Table 1 - Geometrical configuration utilized to test the convergence

Parameter	Value
d	10 [m]
R_1/d	0.001
R_2/d	0.45
R_3/d	0.5
h_1/d	0.2
h_2/d	0.6
h_3/d	0.65
$\Delta\theta$	2π

The convergence study was carried out for fixed geometry and frequency $\omega = 1.5\ [\mathrm{rad/s}]$, analyzing the values of volume excitation flow, radiation damping, and added mass. Convergence for the eigenfunctions in m was achieved immediately such *M* > 2, while convergence for the vertical eigenfunctions was reached for values of *N* > 18, as shown in Figure 11. Hereinafter, the series expansions are truncated at *N* = 20 and *M* = 10, as these values provide accurate estimates across all input frequencies. It is worth mentioning that a similar convergence analysis was performed by varying the number M of eigenfunctions. The numerical results indicated that convergence is achieved with as few as two modes, aligning with comparable numerical studies reported in the literature.

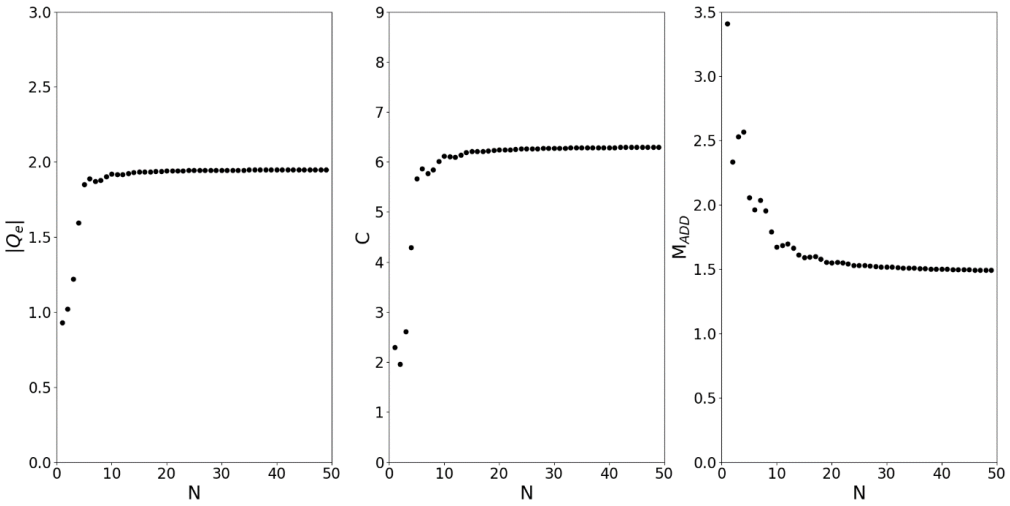

Figure 11 - Convergence study with respect of N for a fixed geometry and frequency $\omega = 1.5$ [rad/s]. Left to right is shown the volume excitation flow, radiation damping and added mass.

Furthermore, an additional analysis was carried out using Haskind's relation, which allows the hydrodynamic characterization to be expressed through the diffracted potential rather than the radiated potential. This approach enables a comparison between the values obtained using the analytical model and those derived from Haskind's relation. The radiation damping formulated throughout Haskind's relation, referring also to the wave incident direction β, is expressed in the following equation:

$$C = \frac{k}{8\pi\rho g c_g A^2} \int_0^{2\pi} |Q_E(\beta)|^2 d\beta \qquad \textbf{(98)}$$

Considering $\beta = 0$, the comparison between these values is shown in Figure 12. It is well depicted the perfect agreement between the values obtained by solving the radiated potential and the Haskind's relation, assessing the reliability of the model.

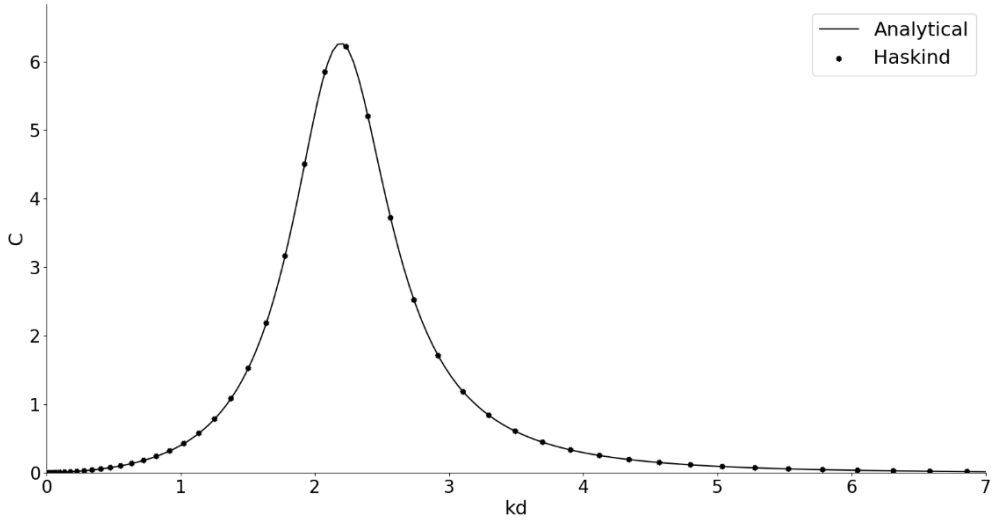

Figure 12 - Comparison between analytical solution and Haskind's relation in terms of Radiation Damping

In the following figures showing the results of the parametric investigations, the limits of the vertical axes have been set based on the maximum value obtained across all plots. This ensures a consistent scale, making all figures immediately comparable.

4.3.2 Effects of the inner chamber width

The width of the device is governed by the dimensions R_2 and R_3. The first parameter describes the width of the internal chamber, while the second represents the overall width of the device; their difference defines the thickness of the wall separating the internal chamber from the external environment. To align with the major studies on cylindrical OWCs, the dimensions provided in the Table 1 are used. The initial analysis considers an internal chamber with an angle of $\Delta\theta = 2\pi$. The internal radius of the device, R_1, is assumed to be small enough not to influence the hydrodynamic properties of the device. The investigation focuses on the influence of the internal chamber width on the device's performance. For this reason, R_3 varies as a function of the internal radius, ensuring constant wall thickness $R_3/d - R_2/d = 0.05$. Three internal radius configurations are considered. One of these approximates a case studied by Michele et al. (2019), which analyzed a similar cylindrical OWC: the nearly perfect overlap of the curves in the corresponding case is further evidence of the reliability of the model

under examination. As shown in Figure 13, increasing the dimensions of the internal chamber results in a change in the peak of the flow rate, damping, and added mass curves in terms of intensity and frequency. In all three cases, an increase in peak values and a shift toward lower frequencies are observed. The added mass graph also includes the M_{PTO} curves, showing that the intersections with the corresponding M_{ADD} curve indicate resonance conditions, which affect the frequencies at which the CWR peaks are reached. No significant changes are observed in the CWR graph aside from translational effects: as the chamber size increases, the CWR peaks shift to lower frequencies and slightly decrease in intensity.

The shift of the peaks to lower frequencies with increasing chamber size is explained by the longer period and consequently longer wavelength of these waves.

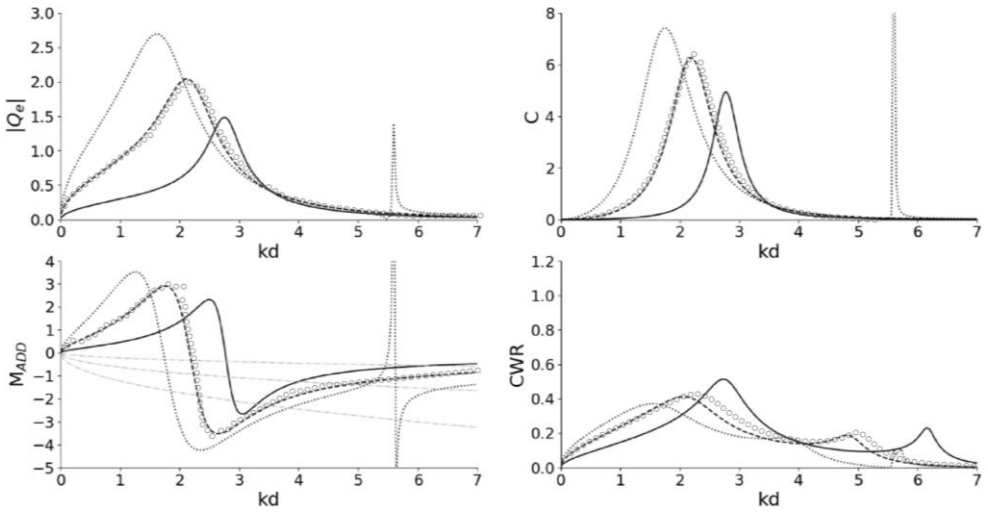

***Figure 13 - Comparison between different radii R_2/d of the OWC chamber. (Continuous line: R_2/d=0.3; dashed line: R_2/d=0.5; dotted line: R_2/d=0.7; circle:** Michele et al. (2019))*

Another parameter that regulates the width of the internal chamber is the radius R_1, which represents the radius of the inner cylinder. Although this structural element is omitted in most cases in the literature, the presence of an inner cylinder ensures greater overall stability of the device, enabling the placement of a lower disc at the height h_2, properly ballasted to ensure buoyancy and stability. As will be discussed later, when analyzing chambers with angles smaller than 2π, the presence of the inner cylinder prevents the

formation of sharp corners. The investigations are conducted by fixing the other parameters to the values shown by the dashed line in Figure 13, while varying the internal radius R_1 across three increasing configurations.

As shown in Figure 14, as long as the radius remains modest-sized, there are no significant changes to the hydrodynamic properties of the device. The situation changes in the third case taken into account, where the inner cylinder's size becomes considerable. The increased size of the inner radius affects the movement of the peaks toward higher frequencies. Additionally, the excitation flow decreases, while peak values of damping and added mass slightly increase. These effects impact the CWR, which shows a reduction in intensity and a shift toward higher frequencies, attributed to the reduction in the size of the internal chamber.

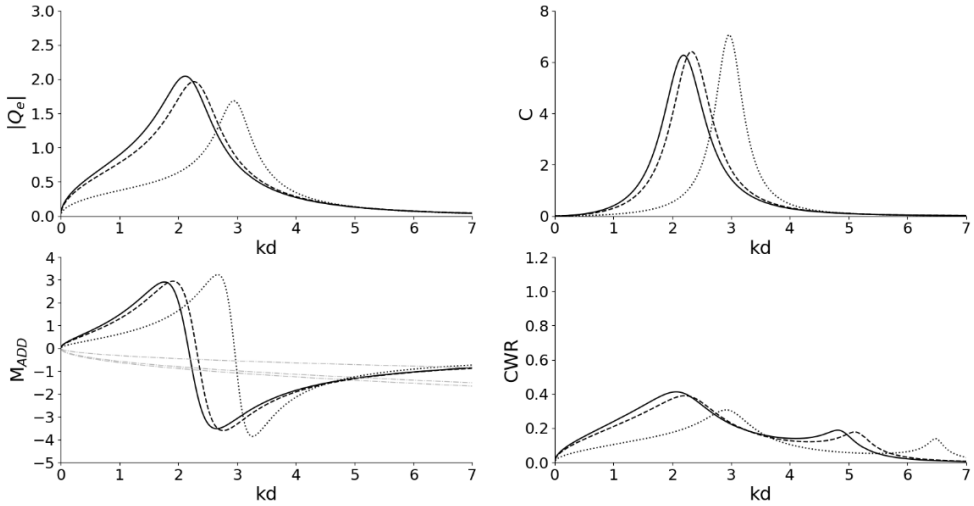

Figure 14 - Comparison between different radii R_1/d of the OWC chamber. (Continuous line: R_1/d=0.001; dashed line: R_1/d=0.15; dotted line: R_1/d=0.35)

4.3.3 Effects of the angular chamber width

One of the main parameters characterizing a cylindrical device is the angle of the internal chamber. In the literature, its symmetry is typically maintained to enable the device to harness wave energy from all directions. However, in reality, we know that wave propagation at any site tends to favor a dominant direction. For this reason, the following analyses have been conducted to evaluate the effects of reducing the angular width of the device. The baseline

configuration used is shown in the following Table 2, corresponding to the dashed line case showed in Figure 14.

Table 2 - Geometrical configuration utilized to test the angular width effects

Parameter	Value
d	10 [m]
R_1/d	0.15
R_2/d	0.5
R_3/d	0.55
h_1/d	0.2
h_2/d	0.6
h_3/d	0.65

Three different angular widths $\Delta\theta = 2\pi;\ \pi;\ \pi/3$ were considered, and the results are presented in Figure 15. Numerical results show immediately that in all three configurations there are no changes in terms of frequency bandwidth, but only in the intensity of the peak, which in some cases is significantly pronounced. The excitation flow increases in the case of a chamber with an angle $\Delta\theta = \pi$, likely due to the occurrence of reflection. This phenomenon arises because the chamber's angle aligns such that its bisector coincides with the propagation direction of the incident waves. As the angular width decreases, a reduction in peak intensity is observed. Damping and added mass exhibit a progressive decrease in amplitude with the reduction of the chamber angle. Interestingly, the reduction in the volume of the internal chamber results also in a decrease in M_{PTO}, as demonstrated by the progressive flattening of the grey dashed curves. Despite this, the intersection with the corresponding M_{ADD} curve remains approximately at the same frequency, related to the reduction in the amplitude of the curve. The effects shown in the previous plots are evident when examining the CWR curves. The increase in excitation flow and the reduction in damping and added mass for the case $\Delta\theta = \pi$ are clearly reflected in the CWR, showing a substantial increase. This trend is also followed by the curve for $\Delta\theta = \pi/3$, which highlights additional advantages, especially at higher frequencies, where the second peak coincides with the curve for $\Delta\theta = \pi$. Moreover, focusing on the first peak, the CWR values reached in the third analyzed case are only about 20% lower than those of the second case. However, the reduced space occupied by this configuration allows for the installation of multiple chambers.

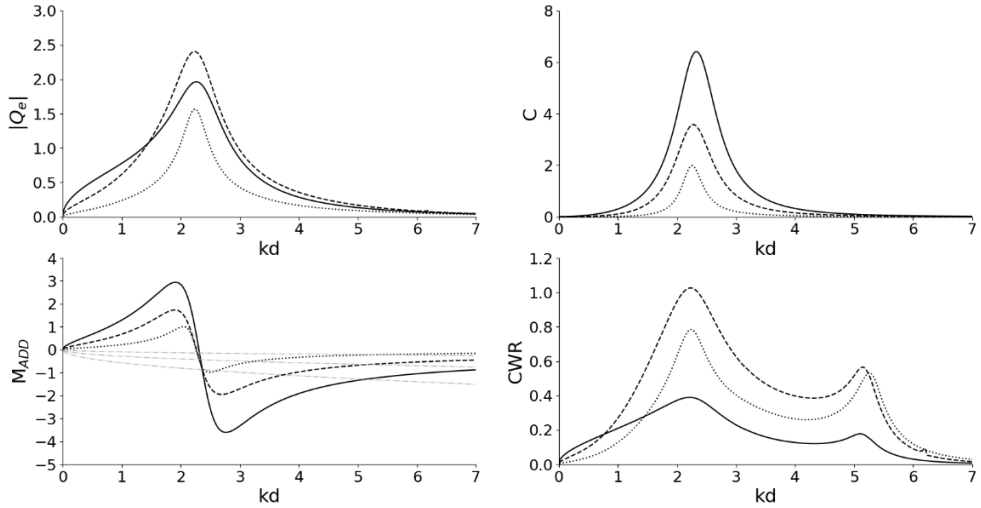

Figure 15 - Comparison between different angle $\Delta\theta$ of the OWC chamber. (Continuous line: $\Delta\theta = 2\pi$; dashed line: $\Delta\theta = \pi$; dotted line: $\Delta\theta = \pi/3$)

4.3.4 Effects of the OWC opening height

The oscillations of the water column inside the device are made possible by the transmission of wave motion forces through the bottom opening. It is crucial to ensure the constant submersion of the wall where the opening is located to guarantee the proper functioning of the device. Moreover, as is well known from potential flow theory, there is a progressive hyperbolic reduction in the kinematic components of wave motion as one moves closer to the seabed. For these reasons, the analysis of the effects of the opening of an OWC was conducted by maintaining a constant submersion depth h_1 of the wall, while progressively increasing the height of the opening toward the seabed. The thickness of the plate at the base is kept constant, so h_3 is defined as a function of h_2 such that $(h_3 - h_2)/d = 0.05$. The geometric configuration used in the investigations corresponds to that reported in Table 2. Based on the results obtained from the studies on the angle of the inner chamber and given that this configuration is not reported in literature, an internal chamber angle of $\Delta\theta = \pi$ is considered. Three analyses were conducted.

The results depicted in Figure 16 show that beyond a certain width, this parameter no longer interferes with the hydrodynamics and energy performance of the device. Indeed, the curves representing the analyses of

the second and third cases are nearly overlapping. The excitation flow rate maintains approximately the same peak value, although it shifts toward higher frequencies as the width of the opening increases. A similar trend is observed for the values of radiation damping and added mass. A slight reduction is also noted in terms of CWR.

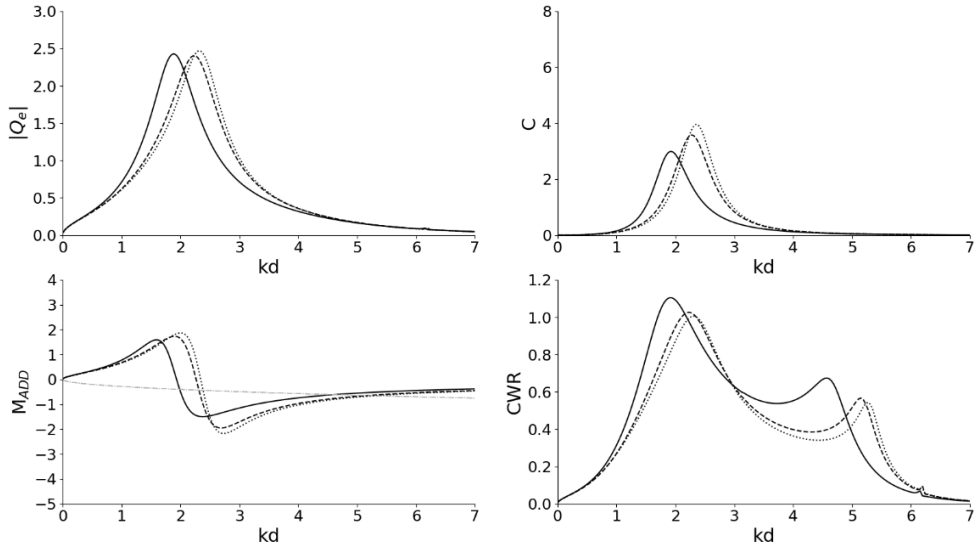

Figure 16 - Comparison between different opening heights of the OWC. (Continuous line: $h_2/d = 0.4$; dashed line: $h_2/d = 0.6$; dotted line: $h_2/d = 0.8$)

The analysis of the height of the opening leads us to conclude that stretching the structure toward the seabed does not result in significant improvements in energy production. Such a design choice is beneficial only for ensuring stability and buoyancy conditions.

4.3.5 Effects of the wall thickness

Commonly, the analytical study of OWC devices is approached under the assumption of thin walls. However, the formulation of the present analytical model allows for investigating the influence of the thickness of the vertical wall on the device's performance. To ensure the comparability of results, the width of the internal chamber is kept constant. The only parameter varied is the external radius R_3. The initial geometry corresponds to that reported in Table 2, with the internal chamber angle set to $\Delta\theta = \pi$. Three wall thickness conditions were taken into analysis.

The results shown in Figure 17 illustrate the influence of this parameter on the device's performance. In the excitation flow rate graph, increasing the thickness results in a progressive shift of the peak toward lower frequencies and higher intensities, accompanied by an overall reduction in frequency bandwidth. A similar trend is observed in the radiation damping curves. The added mass tends to flatten around the inflection point. The energy performance, as indicated by the CWR, reveals a progressive reduction in captured energy with increasing wall thickness. Not only does the first peak decrease, but the second peak also shifts to lower frequencies, causing the curve to narrow and consequently reducing the frequency bandwidth.

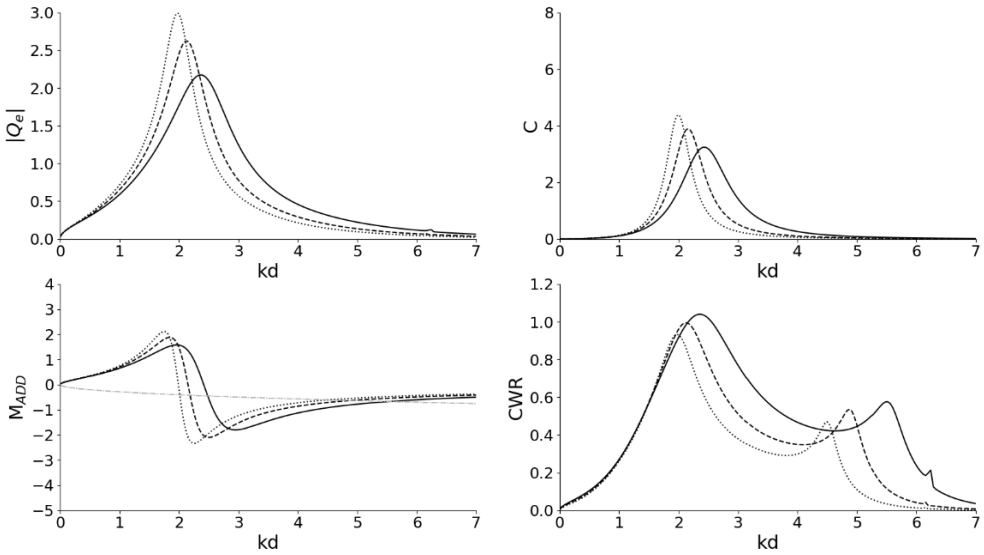

Figure 17 - Comparison between different thickness of the vertical wall. (Continuous line: $R_3/d = 0.51$; dashed line: $R_3/d = 0.6$; dotted $R_3/d = 0.7$)

In conclusion, the thickness of the wall separating the internal chamber from the external environment plays a significant role in the device's energy performance, particularly in terms of frequency bandwidth. For this reason, it should be minimized to ensure structural stability while optimizing the device's efficiency.

4.4 IRREGULAR WAVES

The results presented earlier were obtained under regular wave conditions. In reality, sea waves exhibit an irregular behavior. This representation is

modeled through the theory of sea states. This theory considers a sequence of 100-300 real waves at a fixed point, allowing the process to be treated as stationary and thus representative of real conditions. The elevation of a sea state over time can be analytically represented by summing a sufficiently large number of regular waves, each characterized by amplitudes a_i of the same order of magnitude, a set of distinct frequencies ω_i, and randomly assigned phase angles $\varepsilon_i = [0, 2\pi]$.

$$\eta(t) = \sum_{1=1}^{N} a_i \cos(\omega_i t + \varepsilon_i) \quad \textbf{(99)}$$

Each sea state is associated with a spectrum that graphically represents the energy content of the sea state as a function of frequency. Among the most common spectral models for wind wave representation is the Jonswap spectrum:

$$E(\omega) = Ag^2\omega^{-5}\, exp\left[-1.25\left(\frac{\omega}{\omega_P}\right)^{-4}\right] exp\left\{log(\xi_1)\, exp\left[-\frac{(\omega-\omega_P)^2}{2(\xi_2)^2(\omega_P)^2}\right]\right\} \quad \textbf{(100)}$$

This spectrum is a refinement of the model proposed by Pierson-Moskowitz. It takes into account the Phillips parameter A (linked to the characteristics of the wind generating the waves), the peak frequency ω_P (where the highest energy content of the sea state is observed), and two shape parameters ξ_1 and ξ_2. These parameters typically take the following values:

$$\xi_1 = 3.3 \quad \textbf{(101)}$$

$$\xi_2 = \begin{cases} 0.07 & \omega < \omega_P \\ 0.09 & \omega \geq \omega_P \end{cases} \quad \textbf{(102)}$$

As developed by Michele et al. (2019), considering the amplitude of pressure oscillation inside the chamber P, air density ρ_{AIR}, and the Jonswap spectrum, it is possible to represent the average power available to the turbine $P_{m\,IRR}$ and the power of incident waves under irregular conditions $P_{in\,IRR}$.

$$P_{m\,IRR} = C_{PTO}\,\rho_{AIR}\int E(\omega)\,|P|^2(\omega)\,d\omega \quad \textbf{(103)}$$

$$P_{in\,IRR} = \int \rho g C_g(\omega)\,E(\omega)\,d\omega \quad \textbf{(104)}$$

Consequently, the CWR under irregular wave conditions can be calculated.

$$CWR_{\,IRR} = \frac{P_{m\,IRR}}{D_K\,P_{in\,IRR}} \quad \textbf{(105)}$$

The effects of irregular waves were investigated using the geometric configuration reported in Table 3. The external diameter of the device was considered as the characteristic dimension for the CWR ($D_K = 2R_3$).

Table 3 - Geometrical configuration utilized to test the irregular waves effects

Parameter	Value
d	10 [m]
R_1/d	0.15
R_2/d	0.5
R_3/d	0.55
h_1/d	0.2
h_2/d	0.6
h_3/d	0.65

The results are summarized in Figure 18 through the CWR plot, which also includes the CWR curve corresponding to the regular wave case with the same geometric configuration. The first peak shows a slight reduction in intensity. The main difference lies in the absence of the second peak at higher frequencies.

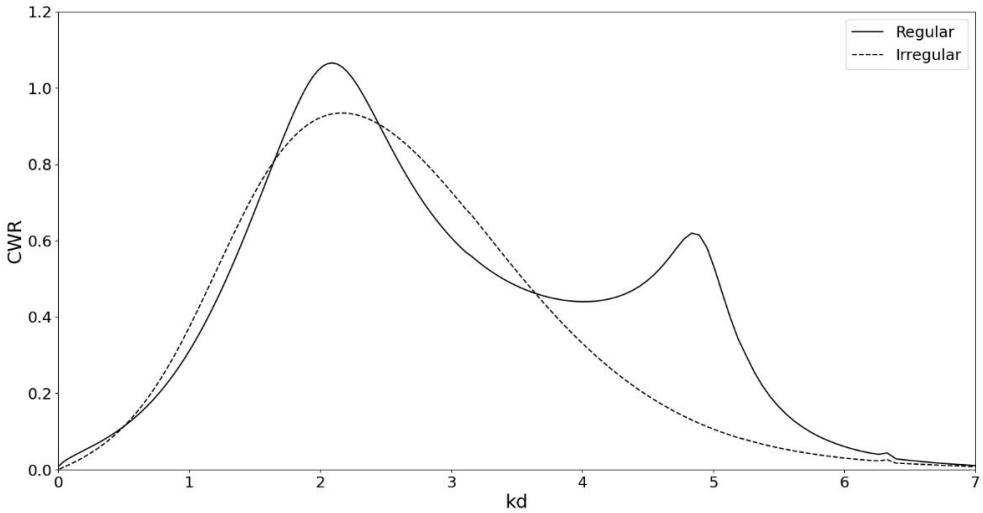

Figure 18 - CWR in irregular waves

In conclusion, we observed that the analysis under regular wave conditions leads to an overestimation of the device's performance, as evidenced by the slightly lower values observed in the case of irregular waves.

CHAPTER 5

Multi-Chamber circular OWC

The optimization of OWC devices is moving toward the implementation of multiple adjacent chambers. The aim is to improve the range of exploitable frequencies and the amount of energy generated by a single device. For this reason, circular OWCs with multiple chambers arranged concentrically along the circular sector have been investigated. However, no studies have explored the possibility of using chambers with reduced angular widths, arranged on the same circular ring.

This chapter presents a semi-analytical solution for a circular OWC with multiple internal chambers on the same circular ring. Specifically, two devices with two and three internal chambers are examined. The results include a direct comparison with the single-chamber configuration.

5 MULTI-CHAMBER CIRCULAR OWC

5.1 GENERAL OVERVIEW

In order to optimize OWC energy performance, recent research has shifted toward innovative multi-chamber devices. Focusing on circular multichambered OWC, Ning et al. (2018) refined the design proposed by Zhou et al. (2018) by introducing a concentric shell and connecting the two chambers at the top of the device. Analyzing surface elevation and energy conversion efficiency, they demonstrated an increase in energy conversion efficiency and an expanded operational frequency bandwidth. Gang et al. (2022) investigated a cylindrical dual-chamber OWC semi-embedded in a breakwater, focusing on the effects of chamber opening angles. The benefits of multi-chamber configurations, with up to five chambers, have been examined numerically and experimentally(Fu et al., 2023; Ning et al., 2024). These studies reveal improved energy efficiency and frequency bandwidth; however, they also demonstrate that increasing the number of chambers beyond a certain point can reduce overall efficiency due to interference effects. Qian et al. (2024) analytically studied a stationary cylindrical offshore OWC with three concentric chambers, highlighting the effects of the number of chambers and key geometrical parameters on device performance.

Parametric studies on cylindrical OWCs conducted by Spanò et al. (2024) have shown that reducing the angular width of the internal chamber leads to a significant increase in energy production. Moreover, the space saved allows for the installation of multiple chambers. An analytical solution, based on potential flow theory, has been developed to investigate the effects of OWCs equipped with multiple chambers positioned within the same circular sector. Two configurations are considered, analyzing the energy performance of devices with two and three chambers, evenly distributed within the cylinder.

5.2 ANALYTICAL MODEL

5.2.1 Geometrical Configuration

Two vertical cylinders equipped with OWC devices are considered. The first consists of two chambers ($N_c = 2$), while the second has three ($\mathrm{N_c} = 3$), as

showed in Figure 19, deployed over constant depth d. In both cases, the chambers share the same angular and radial width, occupying the entire circular sector of the device. A Cartesian coordinate system O_{xyz} is adopted to describe the device. The O_{xy} plane represents the calm sea surface, with incident waves propagating along the x-axis in the opposite direction. The z-axis passes through the vertical axis of symmetry.

The device has a total height defined as h_3 and an external radius equal to R_3. Inside, there is a smaller cylinder with a radius R_1, allowing for the placement of a plate at the base, at a height h_2, to ensure stability and buoyancy. The breakwater wall extends to a submersion depth of h_1, followed by the device's inlet up to the height h_2, designed to transfer wave-induced forces to the inner chamber. Each chamber is characterized by an initial and final angle ($\Delta\theta_{nc} = \theta_{fin-nc} - \theta_{in-nc}$ in which $n_c = [1, N_c]$), calculated from the x-axis, with positive values assigned for counterclockwise directions. The radial width of the chamber is given by the difference $\Delta\mathrm{r} = R_2 - R_1$. All chambers have the same angular $\Delta\theta_{nc}$ and radial $\Delta\mathrm{r}$ dimensions. The $\mathrm{N_c}$ chambers are numbered counterclockwise, starting with the chamber directly impacted by the incident waves. This chamber is positioned such that its bisector aligns with the x-axis, pointing in the direction of the incident waves.

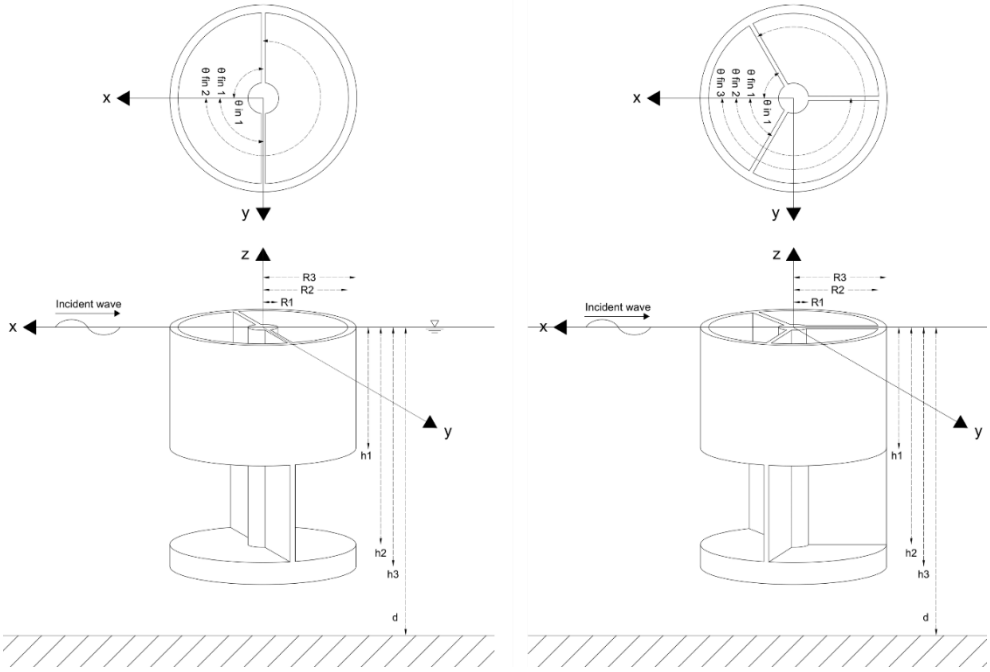

Figure 19 - 3D and top view of the 2-chamber OWC (left) and 3-chamber OWC (right)

5.2.2 Boundary value problem

In order to apply the linearized wave theory and define the velocity potential, the domain is divided into $2 + 2N_c$ sub-domains:

$$\Omega_1(r,\theta,z) = \{\, \mathrm{r} \in [R_3;\ +\infty);\ z \in [-d;\ 0];\ \ \theta \in [0; 2\pi]\}$$

$$\Omega_2(r,\theta,z) = \{\mathrm{r} \in [0;\ R_3]\ ;\ z \in [-d;\ -h_3];\ \ \theta \in [0; 2\pi]\}$$

$$\Omega_{3-n_c}(r,\theta,z) = \left\{r \in [R_1;\ R_2]\ ;\ z \in [-h_2;\ 0];\ \ \theta \in \left[\theta_{in-nc}\ ; \theta_{fin-nc}\right]\right\}$$

$$\Omega_{4-n_c}(r,\theta,z) = \left\{r \in [R_2;\ R_3]\ ;\ z \in [-h_2; -h_1];\ \ \theta \in \left[\theta_{in-nc}\ ; \theta_{fin-nc}\right]\right\}$$

The velocity potential $\phi_{\lambda,i}$ for each i-th sub-domain is calculated by satisfying the boundary value system of equations, regarding both diffracted ($\lambda = D$) and radiated ($\lambda = R$) problems:

$$\nabla^2 \phi_{\lambda,i}\,(r,\theta,z) = 0 \tag{106}$$

$$\frac{\partial \phi_{\lambda,1}}{\partial z} - \frac{\omega^2}{g}\,\phi_{\lambda,1} = 0 \quad at\ z = 0 \tag{107}$$

$$\frac{\partial \phi_{\lambda,3-n_c}}{\partial z} - \frac{\omega^2}{g}\,\phi_{\lambda,3-n_c} = \begin{cases} 0, & at\ z = 0\,,\ \ \lambda = D \\ \dfrac{i\omega P_{n_c}}{\rho g}\,\delta_{r\,n_c}, & at\ z = 0\,,\ \ \lambda = R \end{cases} \tag{108}$$

$$\frac{\partial \phi_{\lambda,i}}{\partial \boldsymbol{n}} = 0 \quad on\ the\ cylinder\ boundary\ and\ seabed \tag{109}$$

$$\lim_{kr\to\infty} \sqrt{r}\left(\frac{\partial \phi_{\lambda,1}}{\partial z} - ik\phi_{\lambda,1}\right) = 0 \tag{110}$$

Into the boundary value problem posed (106)-(110), P_{n_c} represents the air pressure amplitude inside the chamber n_c, ρ is the water density, ***n*** is the unit vector normal to the solid boundary, and $\delta_{r\,n_c}$ is the Kronecker delta function.

5.2.3 Velocity potentials

The velocity potentials for each i-th sub-domain are defined throughout the techniques of separation of variables, eigenfunction expansion and satisfying the equation into the boundary value problem. The results for diffraction $\lambda = D$ and radiation problem $\lambda = R$ are stated into the following equations.

$$\phi_{\lambda,1}(r,\theta,z) = \kappa \sum_{m=0}^{\infty}\sum_{n=0}^{\infty} \alpha_{mn}^{(\lambda,1)} F_{mn}^{(1)}\ cos(m\theta)\,\chi_n^{(1)} + \phi_I \delta_{\lambda D} \tag{111}$$

$$\phi_{\lambda,2}(r,\theta,z) = \kappa \sum_{m=0}^{\infty}\sum_{n=0}^{\infty} \alpha_{mn}^{(\lambda,2)} F_{mn}^{(2)}\ cos(m\theta)\,\chi_n^{(2)} \tag{112}$$

$$\phi_{\lambda,3}(r,\theta,z) = \kappa \sum_{m=0}^{\infty}\sum_{n=0}^{\infty}\Big[\alpha_{mn}^{(\lambda,3A-n_c)}F_{mn}^{(3A-n_c)} + \alpha_{mn}^{(\lambda,3B-n_c)}F_{mn}^{(3B-n_c)}\Big]cos\big[m\beta_{n_c}(\theta-\theta_{in-n_c})\big]\chi_n^{(3)} + \delta_{\lambda R} \quad \textbf{(113)}$$

$$\phi_{\lambda,4}(r,\theta,z) = \kappa \sum_{m=0}^{\infty}\sum_{n=0}^{\infty}\Big[\alpha_{mn}^{(\lambda,4A-n_c)}F_{mn}^{(4A-n_c)} + \alpha_{mn}^{(\lambda,4B-n_c)}F_{mn}^{(4B-n_c)}\Big]cos\big[m\beta_{n_c}(\theta-\theta_{in-n_c})\big]\chi_n^{(4)} \quad \textbf{(114)}$$

The constant $\kappa = \left(-\frac{igA}{\omega}\delta_{\lambda D} - \frac{iP}{\rho\omega}\delta_{\lambda R}\right)$is used to scale the potentials depending on whether the diffraction or radiation problem is being addressed. This distinction is achieved through the use of the Kronecker Delta, $\delta_{\lambda D} = 1$ whenever $\lambda = D$ otherwise $\delta_{\lambda D} = 0$ (same assumptions for $\delta_{\lambda R}$). The Bessel functions are encapsulated in the terms $F_{mn}^{(1)}, F_{mn}^{(1)}, F_{mn}^{(3A-n_c)}, F_{mn}^{(3B-n_c)}, F_{mn}^{(4A-n_c)}, F_{mn}^{(4B-n_c)}$. The parameter β, as reported in equation (32) is used to scale the circular eigenfunctions over the circular domain corresponding to the angular width of the chamber in question. The vertical eigenfunctions are represented by the terms $\chi_n^{(1)}, \chi_n^{(2)}, \chi_n^{(3)}, \chi_n^{(4)}$. The vertical elevations of each chamber are identical, as well as to the single-chamber case studied in the previous chapter. Since the same notation has been used, it is possible to refer to equations (82)-(89)for the calculation of the wavenumbers and vertical eigenfunctions. The terms containing the modified Bessel functions of the first $I_m(k_n r)$ and second kinds $K_m(k_n r)$ are provided below.

$$F_{mn}^{(1)} = \frac{K_m\left(k_n^{(1)}r\right)}{K_m\left(k_n^{(1)}R_3\right)} \quad \textbf{(115)}$$

$$F_{mn}^{(2)}(r) = \begin{cases} \left(\frac{r}{R_3}\right)^m, n = 0 \\ \frac{I_m\left(k_n^{(2)}r\right)}{I_m\left(k_n^{(2)}R_3\right)}, n > 0 \end{cases} \quad \textbf{(116)}$$

$$F_{mn}^{(3A-n_c)} = \frac{I_{m\beta_{n_c}}\left(k_n^{(3)} r\right)}{I_{m\beta_{n_c}}\left(k_n^{(3)} R_2\right)} \quad \textbf{(117)}$$

$$F_{mn}^{(3B-n_c)} = \frac{K_{m\beta_{n_c}}\left(k_n^{(3)} r\right)}{I_{m\beta_{n_c}}\left(k_n^{(3)} R_2\right)} \quad \textbf{(118)}$$

$$F_{mn}^{(4A-n_c)} = \begin{cases} \left(\frac{r}{R_3}\right)^m & n = 0 \\ \frac{I_{m\beta_{n_c}}\left(k_n^{(4)} r\right)}{I_{m\beta_{n_c}}\left(k_n^{(4)} R_3\right)} & n > 0 \end{cases} \quad \textbf{(119)}$$

$$F_{mn}^{(4B-n_c)}(r) = \begin{cases} ln\left(\frac{r}{R_2}\right) + 1 & n = m = 0 \\ \left(\frac{r}{R_2}\right)^{-m} & n = 0;\ m > 0 \\ \frac{K_{m\beta_{n_c}}\left(k_n^{(4)} r\right)}{K_{m\beta_{n_c}}\left(k_n^{(4)} R_2\right)} & n > 0; m > 0 \end{cases} \quad \textbf{(120)}$$

5.2.4 Computation of the unknown terms

The potential unknowns are determined by enforcing the continuity of pressures and velocities along the contact surface between two adjacent domains. These dynamic and kinematic conditions are imposed through the following equations.

$$\left(\phi_{\lambda,1}\right)_{r=R_3} = \left(\phi_{\lambda,2}\right)_{r=R_3} \quad z \in [-d;\ -h_3];\ \ \theta \in [0; 2\pi] \quad \textbf{(121)}$$

$$\left(\phi_{\lambda,1}\right)_{r=R_3} = \left(\phi_{\lambda,4-n_c}\right)_{r=R_3} \quad z \in [-h_2;\ -h_1];\ \ \theta \in \left[\theta_{in-nc}\,; \theta_{fin-nc}\right] \quad \textbf{(122)}$$

$$\left(\phi_{\lambda,3-n_c}\right)_{r=R_2} = \left(\phi_{\lambda,4-n_c}\right)_{r=R_2} \ z \in [-h_2;\ -h_1];\ \theta \in \left[\theta_{in-nc}\,; \theta_{fin-nc}\right] \quad \textbf{(123)}$$

$$\left(\frac{\partial \phi_{\lambda,1}}{\partial r}\right)_{r=R_3} = \begin{cases} \left(\frac{d\partial \phi_{\lambda,2}}{\partial dr}\right)_{r=R_3} & z \in [-d;\ -h_3];\ \theta \in [0; 2\pi] \\ \left(\frac{\partial \phi_{\lambda,4-n_c}}{\partial r}\right)_{r=R_3} & z \in [-h_2; -h_1\ ];\ \theta \in \left[\theta_{in-nc}\ ; \theta_{fin-nc}\right] \\ 0 & z \in [-h_1; 0\ ];\ \theta \in [0; 2\pi] \end{cases} \quad \textbf{(124)}$$

$$\left(\frac{\partial \phi_{\lambda,3-n_c}}{\partial r}\right)_{r=R_2} = \begin{cases} \left(\frac{\partial \phi_{\lambda,4-n_c}}{\partial r}\right)_{r=R_2} & z \in [-h_2;\ -h_1];\ \theta \in \left[\theta_{in-nc}\ ; \theta_{fin-nc}\right] \\ 0 & z \in [-h_1;\ 0];\ \theta \in \left[\theta_{in-nc}\ ; \theta_{fin-nc}\right] \end{cases} \quad \textbf{(125)}$$

The coefficients are determined by projecting the equations onto the space of the vertical eigenfunctions, where the unknown terms are computed as the solution of a linear system of algebraic equations, obtained by truncating the infinite series expansion of the eigenfunctions.

5.3 RESULTS

Numerical analyses conducted on multi-chamber devices require the use of matrix notation for the reference hydrodynamic parameters. The excitation flow rate, derived from solving the diffraction problem, is represented as a vector with dimensions $[1\ x\ N_c]$, whose vector formulation is outlined below.

$$\{\boldsymbol{Q}_E\}_{n_c} = \int_{-\frac{\Delta\theta_{n_c}}{2}}^{+\frac{\Delta\theta_{n_c}}{2}} \int_{R_1}^{R_2} \left(\frac{\partial \phi_{D,3-n_c}}{\partial z}\right)_{z=0} r\ dr\ d\theta \quad \textbf{(126)}$$

Additionally, neglecting the 6 DoF of the cylinder (considered as fixed), the only source of radiation arises from the oscillation of the individual water columns within the chambers. The principle of superposition allows us to

separately study the radiation effects produced by each chamber and then sum the results to observe how the radiation from the various chambers interferes—whether constructively or destructively. The damping and added mass matrices will have dimensions $[N_c\ x\ N_c]$; the rows correspond to the chamber where radiation is considered, and the columns represent the individual chambers, counted counterclockwise starting from the chamber facing the incident waves.

$$\{\boldsymbol{Q}_R\}_{n_c,j} = \{\boldsymbol{P}\}_j \int_{-\frac{\Delta\theta_{n_c}}{2}}^{+\frac{\Delta\theta_{n_c}}{2}} \int_{R_1}^{R_2} \left(\frac{\partial \phi_{R,3-n_c}}{\partial z}\right)_{z=0} r\, dr d\theta = -\left(\{\boldsymbol{C}\}_{n_c j} - i\{\boldsymbol{M}_{ADD}\}_{n_c j}\right)\{\boldsymbol{P}\}_j \quad \textbf{(127)}$$

A full matrix is constructed: the diagonal elements represent the damping and added mass values produced by the radiation activated in the chamber under consideration, while the off-diagonal terms indicate the damping and added mass values observed in adjacent chambers due to radiation from the considered chamber. The radiation problem does not take into account the incident wave. Moreover, is perfectly symmetrical because dealing with chambers of identical geometry. The graphs presented will depict the case where radiation is activated in chamber $n_c = 1$, along with the off-diagonal terms on the same row, representing the hydrodynamic values observed in adjacent chambers due to the radiation in chamber 1. Furthermore, $\{\boldsymbol{M}_{PTO}\}_{n_c n_c}$ is calculated referring to the air volume inside the chamber V_{0,n_c} the polytropic coefficient $\nu = 1.25$. Moreover, following Michele et al. (2019), the optimum value for the PTO radiation damping $\{\mathbf{C}_{\mathrm{PTO}}\}_{n_c n_c}$ is calculated:

$$\{\boldsymbol{M}_{PTO}\}_{n_c n_c} = \frac{\omega V_{0,n_c}}{\nu p_{atm}} \quad \textbf{(128)}$$

$$\{\boldsymbol{C}_{PTO}\}_{n_c n_c} = \sqrt{\{\boldsymbol{C}\}_{n_c n_c}{}^2 + \left(\{\boldsymbol{M}_{PTO}\}_{n_c n_c} + \{\boldsymbol{M}_{ADD}\}_{n_c n_c}\right)^2} \quad \textbf{(129)}$$

All these parameters are expressed in dimensionless form, as proposed by Lovas et al. (2010).

$$\{\overline{\boldsymbol{Q}_E}\}_{n_c} = \frac{\sqrt{g/d}}{A\ d\ g}\ \{\boldsymbol{Q}_E\}_{n_c} \tag{130}$$

$$\left(\{\overline{\boldsymbol{C}}\}_{n_c j}, \{\overline{\boldsymbol{M}}_{ADD}\}_{n_c j}\right) = \frac{\rho\sqrt{g/d}}{d}\ \left(\{\boldsymbol{C}\}_{n_c j}, \{\boldsymbol{M}_{ADD}\}_{n_c j}\right) \tag{131}$$

To better understand the behavior of multi-chamber devices, a study was also conducted on the surface elevation within the device, complemented by a comparison with the respective single-chamber case having the same angular width. This approach allows further evaluation of whether the use of multiple chambers results in constructive or destructive effects in adjacent chambers.

$$\eta\ (r,\theta) = Re\{A\phi_D(r,\theta,0) + \frac{1}{\rho g}\sum_{r=1}^{N_c}\{\boldsymbol{P}\}_r\phi_R\ (r,\theta,0)\} \tag{132}$$

The formulation for calculating the surface elevation within the chambers is performed for a fixed frequency, considering the real part of the diffracted potential multiplied by the amplitude of the incident wave (assumed unitary in this study), and the sum of the individual radiated potentials, each multiplied by the pressure amplitude associated with the respective case.

5.3.1 Validation of the model

To ensure the reliability of the model, a convergence study was performed. The minimum number of terms to be considered in the eigenfunctions was investigated. The geometry considered involves an OWC with two chambers $N_c = 2$ having the same angle, $\Delta\theta_{n_c}$, and the geometric parameters reported in the Table 4.

Table 4 - Geometrical configuration utilized to test the convergence

Parameter	Value
d	10 [m]
R_1/d	0.1
R_2/d	0.5
R_3/d	0.55
h_1/d	0.2

h_2/d	0.6
h_3/d	0.65

The investigations were conducted for a fixed frequency equal to $\omega = 1.35\ [rad/s]$. Figure 20 shows the values of volume excitation flow rate, radiation damping, and added mass for the two chambers as functions of N. As evident from the graphs, $N > 18$ ensures the convergence of the analyzed terms. The same analysis was carried out for the circular eigenfunctions in M, demonstrating immediate convergence.

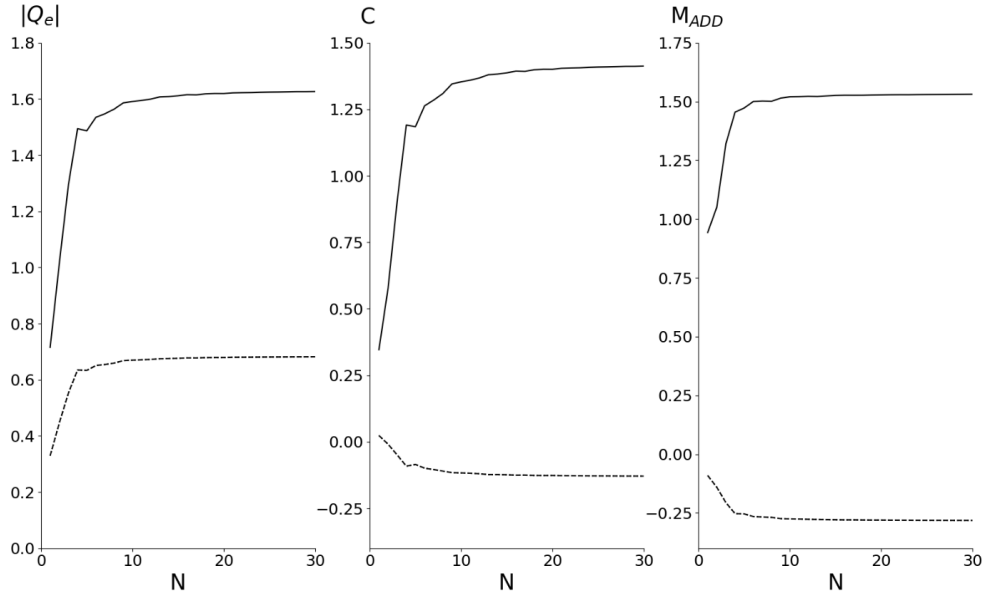

Figure 20 - Convergence study for a fixed geometry and $\omega = 1.35$, in terms of Volume excitation flow, Radiation damping, Added mass (Continuous line: frontal chamber, dashed line: backside chamber)

From this point, $N = 20$ and $M = 10$ will be taken into account for the analyses.

5.3.2 Case A: 2-Chamber OWC

The first case study considered involves a cylindrical OWC equipped with two chambers $N_c = 2$, both characterized by the same angular width, $\Delta\theta_1 = \Delta\theta_2 = \pi$. The device geometry is detailed in the Table 4. The device's performance is presented in Figure 21, where the results are displayed. To

facilitate a comparison with single-chamber devices, the reference curve for a single-chamber OWC with angular width $\Delta\theta = \pi$ and same geometry is also included in the plots. In the radiation damping and added mass plots, the elements of the first row of the matrices are shown, corresponding to the activation of radiation in chamber 1 (facing the waves) and the resulting effects on chamber 2.

As observed in the volume excitation flow rate graph, chamber 1 exhibits a peak elevation compared to the single-chamber case. Chamber 2, on the other hand, has a significantly lower peak, occurring at a slightly lower frequency and quickly approaching zero after the peak value is crossed. The radiation damping shows a slight increase in chamber 1 and takes on negative values in the back-chamber. There are no changes in terms of peak frequency. The added mass curve for chamber 1 closely looks like that of the single-chamber case, whereas the back-chamber's curve displays a mirrored trend along the x-axis, describing a negative peak before. The capture width CW indicates that a multi-chamber device does not alter the frequencies at which the two peaks occur. However, chamber 1 exhibits an increase, particularly in the first peak, while chamber 2's curve has lower values, primarily due to its position.

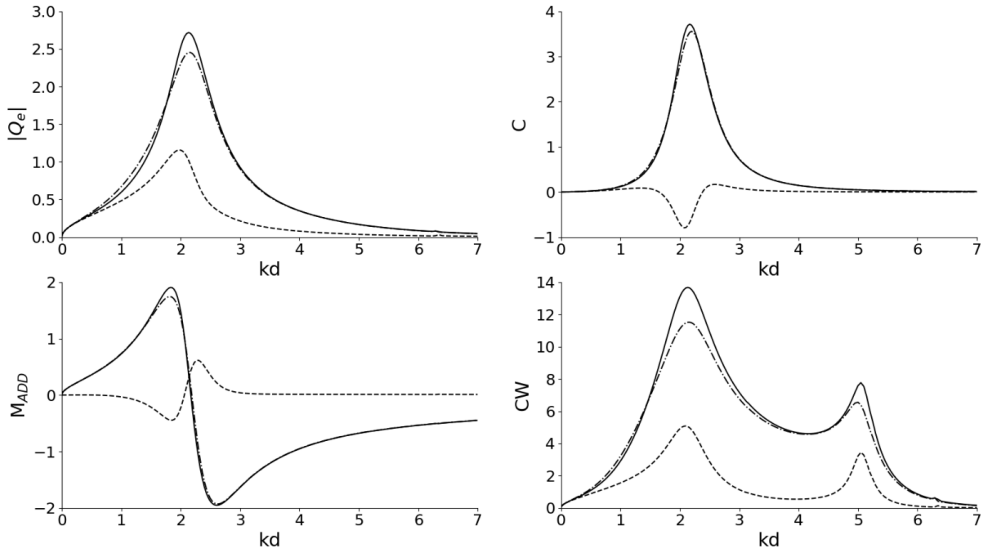

Figure 21 - Double chamber OWC (Continuous line: upwave chamber; dashed line: downwave chamber; dashed-dotted line: single upwave chamber)

In order to better understand the behavior of the device, the surface elevation inside the chambers was also analyzed. To compare the multi-chamber and single-chamber cases, both configurations are shown in Figure 22, keeping the same angular width. The incident waves approach from the right, in the opposite direction to the positive x-axis. The analyzed frequency was selected based on the peak values observed in Figure 21. Specifically, the frequency at which the first peak occurs in the CW plot, equal to $kd = 2.13$ ($\omega = 1.44\ \mathrm{rad/s}$), was chosen. The amplitude of the incident wave is unitary.

Under these conditions, it is observed in the multi-chamber configuration, that the chamber facing the incident waves exhibits an amplification of wave elevation, reaching a peak of $\eta_{max} = 1.6\,m$ near the inner cylinder. In the back chamber, negative values corresponding to the wave trough phase are observed, with a negative peak of $\eta_{max} = -0.8\,m$ near the inner cylinder, and propagating horizontally, almost replicating the diffraction effects generated after the passage of the incident wave. In the single-chamber case, subjected to the same incident wave with unitary amplitude, there is also an increase in wave elevation but with more modest values, represented by a peak of about $\eta_{max} = 1.2\,m$. This comparison highlights how the presence of a

chamber in the back side of the cylinder enhances the properties of the front chamber.

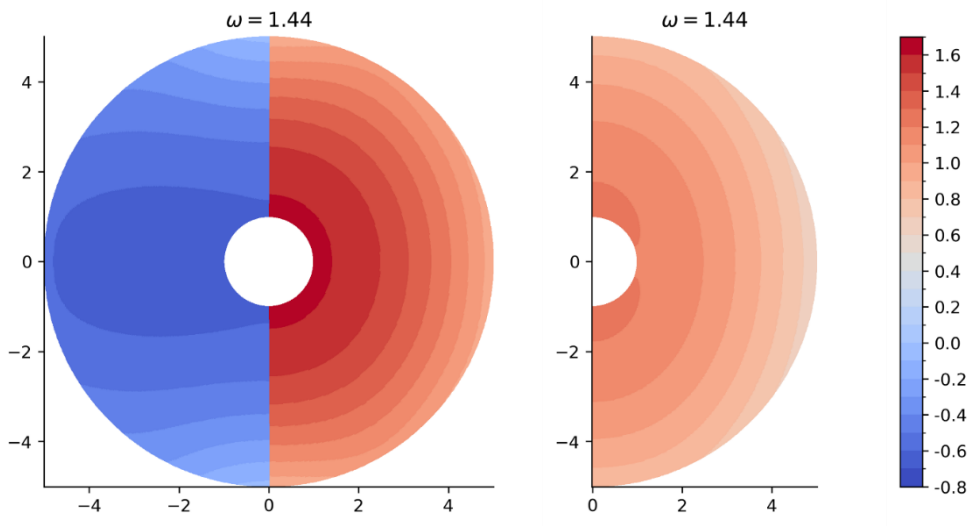

Figure 22 - Surface elevation inside the chamber (Left: multichambered OWC; Right: single chamber OWC). Top view.

5.3.3 Case B: 3-Chamber OWC

The second case study focuses on a vertical cylinder equipped with $N_c = 3$ three inner chambers, each with the same angular width ($\Delta\theta_1 = \Delta\theta_2 = \Delta\theta_3 = 2\pi/3$). These chambers are counted counterclockwise, starting from the one facing the incident waves. The geometry used in the analysis is detailed in the Table 4. The results are presented in Figure 23, depicting the volume excitation flow, radiation damping, added mass, and capture width. The hydrodynamic parameters are obtained by solving the radiation problem caused by the oscillation of the water column inside the device. The plots show the values from the first row of the matrix, which, due to the adopted geometry, is symmetric. Off-diagonal terms are identical, and to avoid confusion, only one curve related to chambers 2 and 3 is shown in the graph. To better compare the effects of multiple chambers, the plots also include the results for a single-chamber cylinder with the same angular width $\Delta\theta = 2\pi/3$ as in the analyzed case.

From the first graph, it can be immediately observed that the volume excitation flow shows an increase in peak intensity, narrowing slightly while remaining at the same frequency as in the single-chamber case. Chambers 2 and 3, on the other hand, exhibit a less pronounced peak due to their position relative to the incident waves. The peak occurs at a slightly lower frequency, and the curve then quickly approaches zero. A similar trend is observed in the graphs of the hydrodynamic parameters. The radiation damping of chamber 1 shows an increase in the peak while remaining at the same frequency. The behavior of the curve representing the back chambers is particularly interesting, displaying a negative peak, likely due to the different wave phase experienced by the chamber. In the added mass graph, chambers 2 and 3 consistently exhibit a less pronounced behavior with an opposite trend: first generating a negative peak, followed by a positive one, and then quickly tending to zero. These effects are reflected in the CW curve. Chamber 1 shows an increase in the first peak, followed by a trend almost corresponding with the single-chamber case, except for a double peak appearing towards the end of the curve. The two back chambers exhibit the same trend as chamber 1 but with much lower values. The increase in the peaks of the various parameters demonstrates how the influence of the rear chambers helps improve the performance of the chamber facing the incident waves.

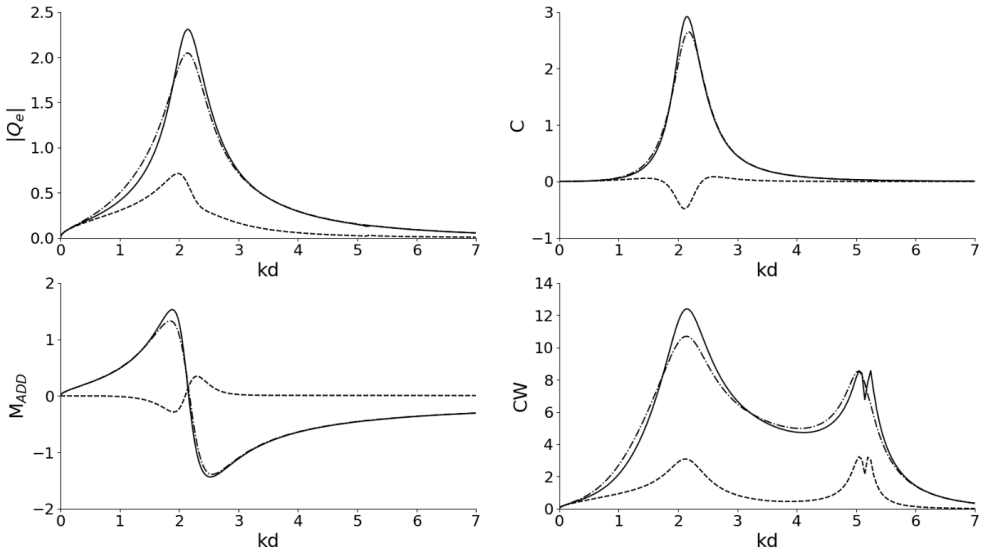

Figure 23 - Triple chamber OWC (Continuous line: upwave chamber; dashed line: both downwave chambers; dashed-dotted line: single upwave chamber)

The study of wave elevation inside the chambers provides further insights into the behavior of the device. Figure 24 presents the results obtained for both the multicamera OWC and the single-chamber OWC. The analyses are conducted for a fixed frequency, the first peak of the CW occurs $(kd = 2.16; \omega = 1.46\ \mathrm{rad/s})$. The incident waves approach from the right side of the plot, in the opposite direction of the positive x-axis. The incident wave is characterized by a unitary amplitude.

In the multi-chamber case, it can be observed that in chamber 1, which faces the incident waves, there is a pronounced amplification of the wave motion, reaching values of $\eta_{max} = 2\ m$ near the inner cylinder. In chambers 2 and 3, however, negative values are observed, corresponding to the wave trough phase. The absolute values in these chambers are smaller, with a maximum of $\eta_{max} = -0.6\ m$, indicating that the majority of the energy content is absorbed by chamber 1. Even in the single-chamber OWC case, wave motion is amplified, reaching levels of $\eta_{max} = 1.2\ m$. However, the values achieved are lower. This comparison demonstrates that the inclusion of multiple chambers tends to enhance the oscillation of the water column in the chamber facing the incident waves.

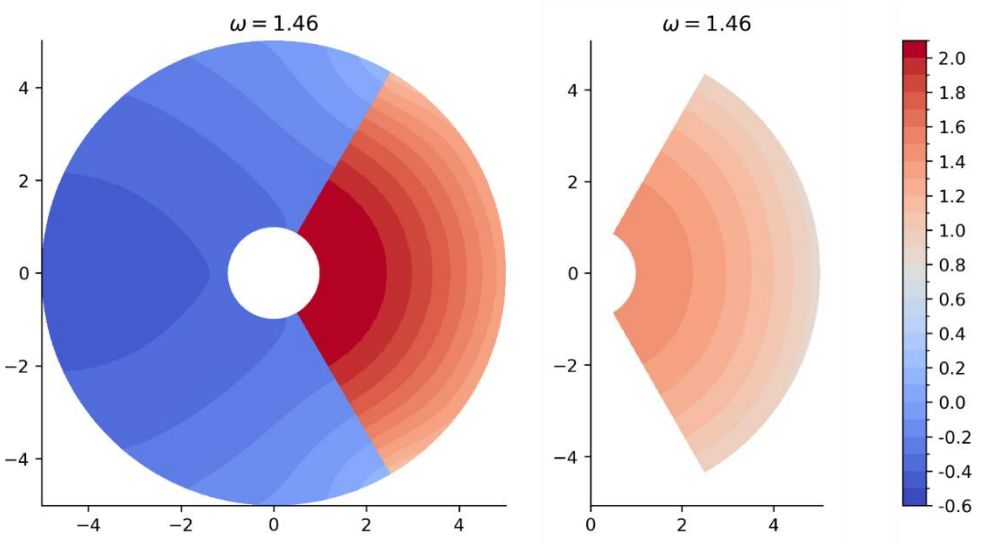

Figure 24 - Surface elevation inside the chamber (Left: multi-chamber OWC; Right: single chamber OWC). Top view

5.4 MULTI-CHAMBER OWC VIS-À-VIS SINGLE-CHAMBER OWC

A comparison between single-chamber and multi-chamber devices is presented here to evaluate whether the use of multiple chambers results in constructive or destructive effects on overall energy performance. This is done by investigating the CW_{total} and introducing two parameters, $r_{factor}(\Delta\theta, \Delta\theta_{single})$ and $q_{factor}(\Delta\theta)$.

$$CW_{total} = \sum_{n_c=1}^{N_c} CW_{n_c} \tag{133}$$

$$r_{factor}(\Delta\theta, \Delta\theta_{single}) = \frac{CW_{total}(\Delta\theta)}{CW_{single}(\Delta\theta_{single})} \tag{134}$$

$$q_{factor}(\Delta\theta) = \frac{CW_{total}(\Delta\theta)}{N_c\, CW_{single}(\Delta\theta)} \quad \textbf{(135)}$$

5.4.1 Comparison in terms of CW

The parameter that summarizes the device's performance is the capture width, as it represents the ratio between the mean power available to the turbine and the incident power. This value was referred to individual chambers in previous case studies. To obtain a comprehensive response for a device with multiple chambers, the CW_{total} is calculated.

Figure 25 compares the CW obtained for a single-chamber device (left panel), varying the angular width of the chamber, and the CW_{total} (right panel) for devices with $N_c = 2$ and $N_c = 3$ chambers, each with the same angular width. Single-chamber devices show a significant increase in performance for chambers with reduced angular widths, as seen from the first peak. Moreover, as shown by the dotted curve corresponding to $\Delta\theta = 2\pi/3$, further reducing the chamber's angular width allows better utilization of the energy contained at higher frequencies. By adopting the same scale for the ordinate values, an immediate comparison can be made with the CW_{total} values obtained for multi-chamber devices. Additionally, the line style matches that of the single-chamber case with the same angular width. A substantial increase in the two peaks is immediately noticeable, demonstrating that OWC devices can be further optimized not only by reducing the chamber's angular width but also by utilizing the additional space to install extra chambers, which contribute to producing additional energy.

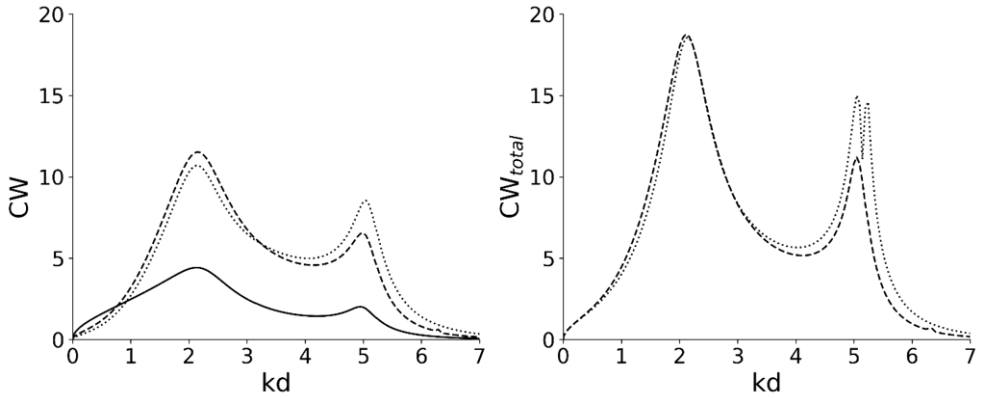

Figure 25 - CW of a single-chamber OWC (left) and CW_{total} of multi-chamber OWC (right). (Continuous line: $\Delta\theta = 2\pi$; dashed line: $\Delta\theta = \pi$; dotted line: $\Delta\theta = 2\pi/3$)

5.4.2 Comparison in terms of r-factor

The $r_{factor}(\Delta\theta, \Delta\theta_{single})$ represents the ratio between the sum of the CW values of the individual chambers in a multi-chamber OWC and the CW of a single-chamber device. It is used to demonstrate the relative efficiency of a multi-chamber OWC compared to a single-chamber one in terms of CW. To further deepen the comparison, it is possible to evaluate OWCs where the single chamber assumes different values $\Delta\theta_{single}$ than those adopted in the multi-chamber case.

The multi-chamber configurations analyzed in the previous case studies, $N_c = 2$ and $N_c = 3$, were used as the basis for the following comparisons. These devices were evaluated against the most established design in the literature for cylindrical OWCs, which features a single internal chamber with an angular width of $\Delta\theta = 2\pi$. As shown in Figure 26, the $r_{factor}(\Delta\theta, 2\pi)$ value approaches 1 at low frequencies before beginning to increase. The two curves are nearly identical up to the frequency $kd = 3.09$, where they exhibit a productivity peak four times higher than the classic cylindrical OWC with a single internal chamber covering the entire circular sector. At higher frequencies, the multi-chamber configuration demonstrates improved efficiency, highlighting the advantage of dividing the device into multiple chambers.

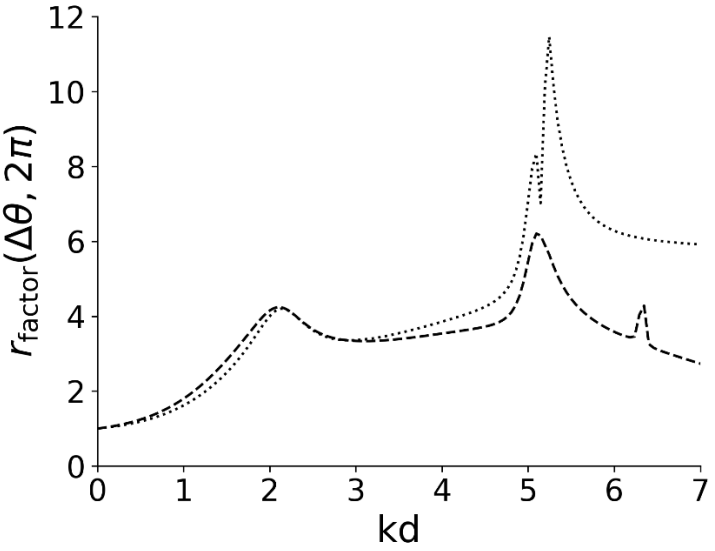

Figure 26 - r_{factor} concerning $\Delta\theta = \pi$ (Nc=2, dashed line) and $\Delta\theta = 2\pi/3$ (Nc=3, dotted line), against a single chamber OWC with $\Delta\theta_{single} = 2\pi$

The optimal configuration for a single-chamber cylindrical OWC, as demonstrated by Spanò et al. (2024) and shown in Figure 25, involves reducing the internal chamber's angular width to $\Delta\theta = \pi$. To further analyze, the $r_{factor}(\Delta\theta, \pi)$ was taken into account, comparing the two previously investigated multi-chamber cases with the optimized single-chamber OWC. The results are presented in Figure 27. The curve consistently remains above 1, indicating that the presence of multiple chambers constructively enhances the overall performance of the device. The results reveal that at very low frequencies, the efficiency is doubled, attributed to the piston-like motion of the water column. The first peak already highlights this positive trend. Additional benefits are observed at higher frequencies, where the difference becomes more pronounced.

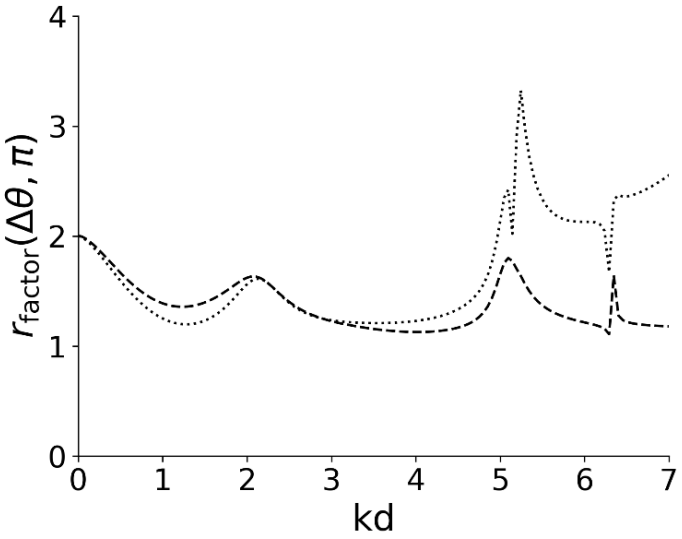

Figure 27 - r_{factor} concerning $\Delta\theta = \pi$ (Nc=2, dashed line) and $\Delta\theta = 2\pi/3$ (Nc=3, dotted line), against a single chamber OWC with $\Delta\theta_{single} = \pi$

An interesting observation arises from a comparison with the Figure 26: the values in the current graph are lower, further demonstrating that an OWC with $\Delta\theta = \pi$ is superior to one with $\Delta\theta = 2\pi$ in terms of energy efficiency. Furthermore, cylindrical OWCs can be further optimized not only by reducing the angular width of the internal chamber but also by incorporating additional chambers, whose interactions positively impact the device's overall performance.

5.4.3 Comparison in terms of q-factor

The $q_{factor}(\Delta\theta)$, highlights the efficiency of a multi-chamber device compared to an array of single-chamber devices. It is calculated as the ratio between CW_{total} and the product of the number of chambers and the CW of a single-chamber OWC with the same angular width.

The results are presented in Figure 28, regarding devices with $N_c = 2$ (solid line) and $N_c = 3$ (dashed line). It is immediately showed that the curve remains below unity, indicating that a single device with N_c chambers will

never achieve the same efficiency as N_c separate devices, each equipped with a single chamber of the same angular width. After an initially common segment, the two curves settle into a nearly parallel trajectory, with an approximate difference of 0.2. From these curves, we can conclude that a device with $N_c = 2$, if properly designed, can achieve an energy efficiency ranging from 60% up to 80% compared to two separate OWCs with a single internal chamber of $\Delta\theta = \pi$. Similar considerations apply to the case of $N_c = 3$, where the performance of an OWC equipped with three chambers falls within a range of 39% to 78% compared to three cylindrical OWCs, each with a single chamber of $\Delta\theta = 2\pi/3$. These results further underscore the benefits of devices equipped with multiple chambers.

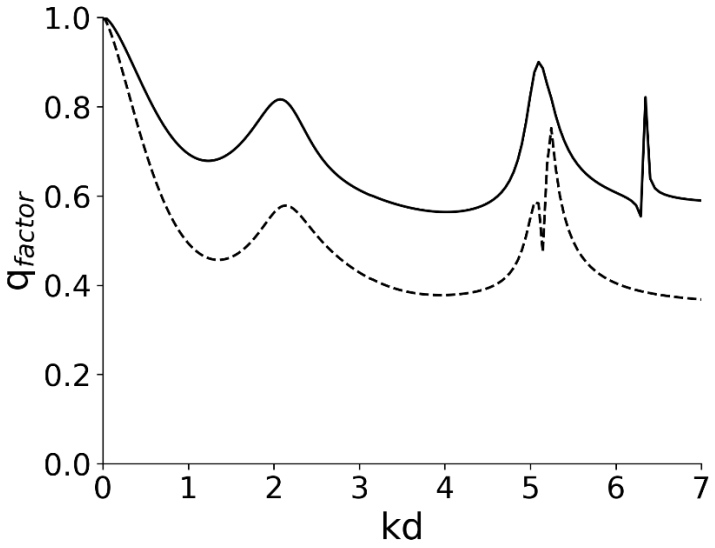

Figure 28 - q_{factor} (Continuous line: Nc=2; dashed line: Nc=3)

CHAPTER 6

Applicative Study Case

The design of an OWC is closely related to the specific site taken into account. Each location is characterized by unique energy conditions, determined by the local wave climate in terms of wave height, period, and direction. The goal of OWC design is to align the device's productivity peaks with the energy peaks of the chosen site.

This chapter provides a short example of the workflow for designing an OWC. The selected site is Mazara del Vallo (Italy), recognized as one of the most energetic sites within the Italian seas. The chapter begins with an energy assessment of the location, followed by the geometrical selection of the device and an analysis of its overall energy production.

6 CASE STUDY

The design of a cylindrical OWC must align with the energy-favorable conditions of the selected site to optimize energy conversion. The preliminary investigation requires a comprehensive wave resource assessment. Once the most relevant wave conditions in terms of frequency and energy are identified, a parametric study is conducted to determine the geometric dimensions of the OWC, in order to ensure optimal operative conditions within the relevant climate conditions. After identifying the geometry, the power and annual energy output of the device are calculated and compared to the energy of the incident waves, thereby assessing the device's conversion efficiency.

6.1 MAZARA DEL VALLO TEST SITE

For the proper design, management, and maintenance of maritime structures and infrastructures, it is essential to have a dataset capable of describing wave climate conditions. Since 1989, Italy has developed a maritime meteorological monitoring system, managed by ISPRA since 2008. This system primarily consists of the network named Rete Mareografica Nazionale (RMN, measuring tide elevation), with 36 stations (2024) mostly located within port infrastructures, and the second network called Rete Ondametrica Nazionale (RON), comprising 10 wave buoys (2024) positioned offshore at key locations in Italian seas, as showed in Figure 29 and reported in Table 5. The wave buoys record sea states, measuring significant wave height, mean period, peak period, and wave direction. The acquired data is open access.

Figure 29 - Data buoys Italian network (www.mareografico.it)

Table 5 – Italian Buoy Location

Name	Lat	Lon	Depth [m]
Alghero	40° 32’ 55’’N	08° 06’ 25’’E	85
Ancona	43° 49’ 26’’N	13° 43’ 10’’E	70
Civitavecchia	42° 14’ 41’’N	11° 33’’ 14’’E	62
Crotone	39° 01' 25’’N	17° 13' 12’’E	80
La Spezia	43° 55’ 45’’N	09° 49’ 40’’E	85
Mazara del Vallo	37° 31’ 05’’N	12° 32’ 00’’E	85
Monopoli	40° 58’ 30’’N	17° 22’ 40’’E	85
Ponza	40° 52’ 00’’N	12° 57’ 00’’E	115
Ragusa	37° 26’ 24’’N	15° 08’ 48’’E	90
Venezia	45° 20’ 00’’N	12° 31’ 00’’E	17

Mazara del Vallo, identified as one of the locations with the highest energy potential, has been selected as the site for designing an OWC system. The data considered for this purpose includes records spanning from 1990 to 2014, amounting to a total of 157 471 data. Each record reports values for

significant wave height, mean period, peak period, and wave (incoming) direction. The initial data analysis focused on counting the number of occurrences within circular sectors of a fixed width of 30°. The majority of waves originate from two primary sectors. As shown in Figure 30, 38.62% of sea states come from the 270°-299° sector, named hereinafter sector A, while 17.06% come from the 120°-149° sector, called sector B. The angular offset between these two main sectors is 120°, which led to the decision to design a device with three chambers, positioned to face the incoming waves perpendicularly.

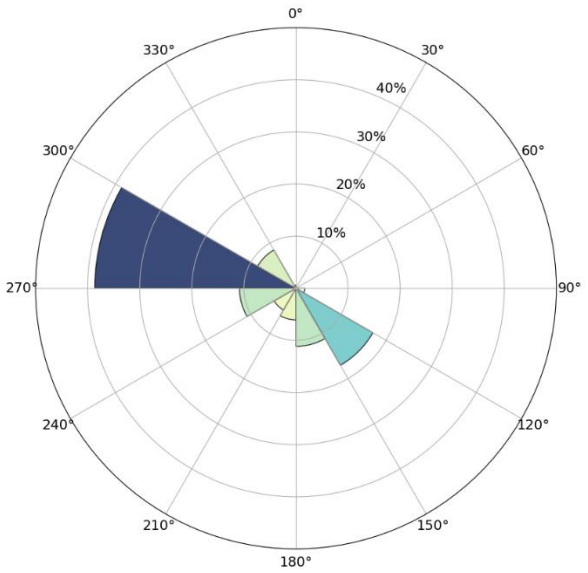

Figure 30 - Fraction of sea states in Mazara del Vallo within 30° circular incoming direction sectors

Once the circular sectors for the device's operation are determined, the corresponding power matrices were developed. These matrices represent the annual energy of incident waves as a function of specific ranges of wave height and period. The energy is calculated as the product of the incident power, determined using equation (136), the number of occurrences, and the annual hours.

$$P_{INC} = \frac{1}{8}\rho g C_g H^2 \qquad \textbf{(136)}$$

The incident power is expressed in *W/m* and depends on the water density ρ and the square of the wave height H. The group velocity C_g is calculated under the assumption of deep water conditions, given a depth $d = 85\ m$. For this reason, regarding the wave period T, the group velocity is determined as follows:

$$C_g = \frac{gT}{4\pi} \qquad \textbf{(137)}$$

Considering the three scenarios with the highest energy availability from the incident waves, it is observed that in both matrices these conditions occur when $\boldsymbol{H}$ is between 1 and 2.5, and the period ranges between 4 and 6.

Table 6 - Power matrix Sector A

E_{INC} [kWh/m per year] DIR 270° 299°

Hs	0	0,5	1	1,5	2	2,5	3	3,5	4	4,5	5	5,5	6	6,5
Tm	0,5	1	1,5	2	2,5	3	3,5	4	4,5	5	5,5	6	6,5	7
0 2	0,00	-	-	-	-	-	-	-	-	-	-	-	-	-
2 4	46,47	440,72	128,76	0,28	-	-	-	-	-	-	-	-	-	-
4 6	18,91	820,94	2.661,36	3.356,67	2.618,86	1.445,27	286,33	10,59	-	-	-	-	-	-
6 8	0,70	63,80	347,55	903,97	1.278,71	1.737,96	2.071,09	1.639,60	959,68	566,09	168,53	13,94	-	-
8 10	0,30	3,51	22,03	32,38	50,78	135,30	183,25	247,78	215,44	587,15	373,58	206,14	31,77	24,70
10 12	0,04	0,37	-	-	-	-	-	9,32	5,98	-	45,66	76,68	25,88	30,19
12 14	0,02	0,44	-	-	-	-	-	-	-	-	-	-	-	-
14 16	0,03	0,25	-	-	-	-	-	-	-	-	-	-	-	-
16 18	-	-	-	-	-	-	-	-	-	-	-	-	-	-
18 20	-	-	-	-	-	-	-	-	-	-	-	-	-	-
20 22	-	-	-	-	-	-	-	-	-	-	-	-	-	-

Table 7 - Power matrix Sector B

E_{INC} [kWh/m per year]		DIR	120°	149°											
Hs		0	0,5	1	1,5	2	2,5	3	3,5	4	4,5	5	5,5	6	6,5
Tm		0,5	1	1,5	2	2,5	3	3,5	4	4,5	5	5,5	6	6,5	7
0	2	-	-	-	-	-	-	-	-	-	-	-	-	-	-
2	4	20,02	310,40	356,64	12,45	-	-	-	-	-	-	-	-	-	-
4	6	7,69	257,44	883,36	1404,84	891,25	585,40	160,66	10,59	-	-	-	-	-	-
6	8	0,59	32,26	105,09	249,24	369,31	460,80	492,16	367,65	182,80	118,93	40,68	13,94	-	-
8	10	0,10	1,68	6,35	12,45	15,10	18,45	31,50	19,06	24,48	42,81	14,94	-	-	-
10	12	0,04	0,19	-	-	1,68	5,01	-	-	-	-	-	-	-	-
12	14	0,02	-	-	-	-	-	-	-	-	-	-	-	-	-
14	16	0,03	-	-	-	-	-	-	-	-	-	-	-	-	-
16	18	-	-	-	-	-	-	-	-	-	-	-	-	-	-
18	20	-	-	-	-	-	-	-	-	-	-	-	-	-	-
20	22	-	-	-	-	-	-	-	-	-	-	-	-	-	-

6.2 PARAMETRIC ANALYSIS

Based on the investigations through the directionality of sea states, their frequency, and energy content, it was agreed to install a device with three chambers spanning the circular sector. Once the type of multi-chamber OWC was defined, the next step involved the proper design of the geometric components to position the peak of the device's energy performance within the frequency range identified as energetically advantageous. In this case, the period range was identified as between $T = 4\,sec$ and $T = 6\,sec$, which corresponds to frequencies denoted as $\omega = 1.04\,[rad/sec]$ and $\omega = 1.57\,[rad/sec]$. To demonstrate how geometry significantly influences the productivity of an OWC, three parametric studies are presented below, considering three different geometries. The main parameter affecting the lateral shift of the peak values of the investigated quantities - such as

excitation flow, radiation damping, added mass, and capture width - is the radial amplitude of the chamber. Keeping the vertical dimensions constant, the three configurations are shown in the Table 8.

Table 8 – Geometrical investigation OWC

[m]	**CASE A**	**CASE B**	**CASE C**
$\boldsymbol{d}$	89	89	89
$\boldsymbol{R_1}$	1	2	3
$\boldsymbol{R_2}$	5	7	9
$\boldsymbol{R_3}$	5.5	7.5	9.5
$\boldsymbol{h_1}$	3	3	3
$\boldsymbol{h_2}$	7	7	7
$\boldsymbol{h_3}$	8	8	8
$\boldsymbol{\Delta\theta}$	$2\pi/3$	$2\pi/3$	$2\pi/3$
Colour	Red	Green	Blue

The results are shown in Figure 31. In the graphs, two dashed purple vertical lines mark the frequency bandwidth within which the device should be operative. The three configurations are distinguished by colour. Each case features a solid line representing the chamber facing the incident waves and a dashed line depicting the behaviour inside the other chambers. Due to the symmetry of the structure, the performance of the two back chambers is identical, resulting in overlapping curves. For the hydrodynamic parameters of radiation damping and added mass, the off-diagonal terms are displayed. The three configurations demonstrate that a larger chamber size enables better utilization of the energy potential of waves with longer periods and higher energy content. Referring to the blue curve, representing configuration C, it is identified as the most effective for harnessing energy potential. This is particularly evident in the capture width graph, where the area under the curve is greater than in the other configurations. Configuration C is therefore selected.

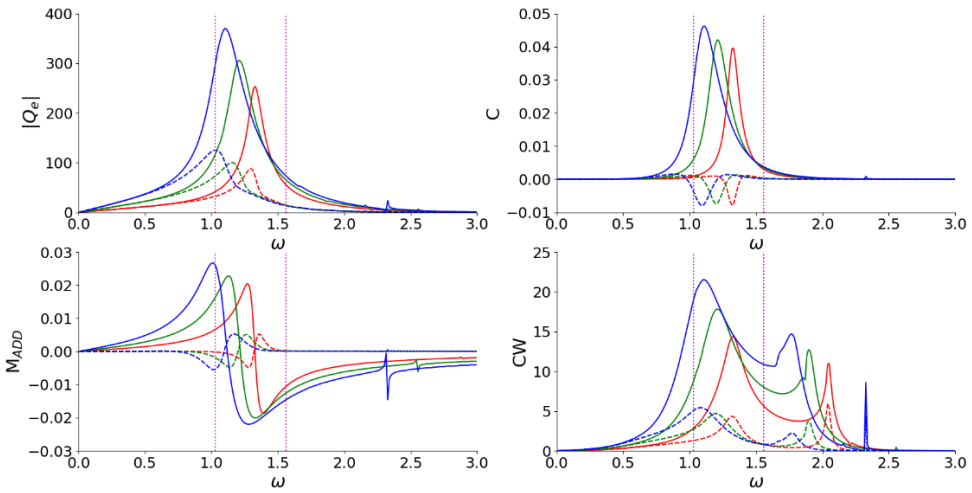

Figure 31 - Parametric investigation towards

6.3 ENERGY PERFORMANCE

The device's energy performance is evaluated by considering the average power and annual energy available to the turbine, obtained by summing the contributions of all the three chambers. Due to the circular shape of the vertical structure, the incident power is calculated based on the portion of the device in contact with the waves, specifically the external perimeter of the cylinder. The energy production analysis is limited to the two sectors identified as containing the highest energy amount of the wave climate recorded by the Mazara del Vallo wave buoy. For each of these sectors, the wave conditions with the highest energy content, in terms of significant wave height H_s, mean period T_m, and frequency of occurrence f, were considered.

As shown in Table 9, examining the values of the incident wave energy confirms that the 270° - 299° sector is the most energy. Additionally, it is observed that a higher frequency of occurrence does not necessarily correspond to the highest energy content. The maximum condition occurs in the 270° - 299° sector with $H_s = 1.75\ m$ and $T_m = 5\ sec$, where the average energy available to the turbine reaches $E_{TURB} = 138\ MWh/year$.

Table 9 - Energy Performance

Sector	H_s	T_m	f	P_{INC}	E_{INC}	P_{TURB}	E_{TURB}
	[m]	*[s]*	*[%]*	*[kW]*	*[MWh/year]*	*[kW]*	*[MWh/year]*
270°-299°	1,25	5	7,18%	450,87	283,67	175,83	110,63
270°-299°	1,75	5	4,62%	883,71	357,79	341,82	138,39
270°-299°	2,25	5	2,18%	1460,82	279,14	569,69	108,86
120°-149°	1,25	5	2,38%	450,87	94,16	175,83	36,72
120°-149°	1,75	5	1,93%	883,71	149,74	341,82	57,92
120°-149°	2,25	5	0,74%	1460,82	95,00	569,69	37,05

The overall contribution of the device can be obtained by summing up all circular sectors and all combinations from the power matrix. This case study is focused on demonstrating a computational workflow for designing, optimizing, and evaluating the energy performance of a cylindrical multi-chamber OWC device. Finally, a comprehensive assessment of the device is provided by summing the energy of the incident waves, the energy available to the turbine, and the ratio between these two quantities. The results are presented in the Table 10. The data indicates that only 19% of the sea states were considered in evaluating the device's energy performance. Considering the total of incident wave energy occurring at the device of $E_{INC-TOT} = 1260\, MWh/year$, the device achieve a total energy output of $E_{TURB-TOT} = 490\, MWh/year$. Comparing the two values yields at $\hat{\boldsymbol{\eta}} = \mathbf{39}\%$ as production ratio. However, it should be noted that these calculations were based on a regular wave field, and the energy production is assessed net of the turbine used.

Table 10 - Global Energy Performance

f	$E_{INC-TOT}$	$E_{TURB-TOT}$	$\hat{\eta}$
[%]	*[MWh/year]*	*[MWh/year]*	*[%]*
19%	1260	490	39%

CHAPTER 7

Concluding Remarks

7 CONCLUDING REMARKS

Being reducing emissions and meeting the growing energy demand priorities, the exploitation of renewable energy sources is fundamental. The potential contribution of wave energy stands out as a significant contributor to the transition and diversification of energy supply. Specifically, the Oscillating Water Column (OWC) technology represents one of the most promising solutions for converting wave energy into clean energy. However, the primary limitation to industrial-scale deployment is the lack of convergence towards a single device type.

This study focuses on vertical cylinders equipped with OWCs. A semi-analytical formulation was developed to investigate its behavior using potential flow theory. Each subdomain was characterized by a velocity potential represented by eigenfunction expansions with unknown coefficients. The unknown coefficients were determined by using the matching technique. The linear approach to the problem enabled preliminary investigations of the devices under consideration.

Initially, a single-chamber cylinder was taken into account. The analytical solution allowed investigating the role of individual geometric components. The results, in terms of excitation flow rate, radiation damping, added mass and capture width, revealed that increasing the radial dimensions of the inner chamber shifts the performance peak to lower frequencies, thereby better harnessing the energy potential of longer-period waves. The presence of an inner cylinder does not significantly affect the overall performance. Notably, the angular width of the chamber emerged as a critical parameter: reducing it leads to increased productivity while maintaining the same operating frequency bandwidth. The depth of the chamber's opening showed minimal impact on the device behavior, whereas the outer cylinder thickness reduces internal movement, consequently lowering its performance.

The promising results regarding reduced angular-width chambers prompted further investigation. A semi-analytical solution was developed for cylindrical OWCs equipped with multiple reduced angular-width chambers. The two cases analyzed, featuring two and three chambers, demonstrated that the chamber facing the incoming waves experiences increased energy productivity due to the presence of adjacent chambers. This result is evident

from the presented graphs, which compare the performance of a single-chamber OWC with the same angular width. Further insights were provided by comparing wave elevation within the devices. An additional comparison between multi-chamber and single-chamber systems introduced two parameters: $r_{factor}(\Delta\theta, \Delta\theta_{single})$ and $q_{factor}(\Delta\theta)$. The $r_{factor}(\Delta\theta, \Delta\theta_{single})$ measures the total capture width of a multi-chamber system relative to that of a single-chamber device, highlighting the clear advantage of using multiple chambers. The $q_{factor}(\Delta\theta)$ compares the performance of a single multi-chamber device to an array of single-chamber devices, showcasing the energy competitiveness between the two configurations.

A case study concludes this thesis by implementing the previously discussed considerations. The study aimed to give a qualitative estimate of the overall energy production of an optimized cylindrical OWC. The selected site is Mazara del Vallo, where wave data from the Italian RON wave monitoring service buoy are available. The analysis revealed that the two main energetic wave sectors are 270° - 299° and 120° - 149°. With a 120° angle between the two sectors, a cylinder with three chambers was identified as the optimal solution for the site. From the formulation of a power matrix, it was observed that both sectors exhibit peak energy conditions for sea states characterized by a period T_m between 4 and 6 seconds. Based on this range, parametric investigations were conducted to position the device's energy peak within this frequency band. After optimizing the geometry, the three most energetic sea states for the two main sectors were selected. These account for only 20% of the annual wave occurrences. Considering the total net energy production (without turbine losses), the device demonstrated an annual production of approximately 490 MWh, with a productivity index of 39% relative to the incident wave energy.

BIBLIOGRAPHY

Abbas, S.M., Alhassany, H.D.S., Vera, D., Jurado, F., 2023. Review of enhancement for ocean thermal energy conversion system. Journal of Ocean Engineering and Science 8, 533–545. https://doi.org/10.1016/J.JOES.2022.03.008

Arena, F., Romolo, A., Malara, G., Fiamma, V., Laface, V., 2017. The First Full Operative U-OWC Plants in the Port of Civitavecchia. https://doi.org/10.1115/OMAE2017-62036

Arvizu, D., Balaya, P., Cabeza, L.F., Hollands, K.G.T., Jäger-Waldau, A., Kondo, M., Konseibo, C., Meleshko, V., Stein, W., Tamaura, Y., Xu, H., Zilles, R., Aberle, A., Athienitis, A., Cowlin, S., Gwinner, D., Heath, G., Huld, T., James, T., Kazmerski, L., Mann, M., Matsubara, K., Meier, A., Mujumdar, A., Oozeki, T., Sanogo, O., Santamouris, M., Sterner, M., Weyers, P., Calvo, E., Schmid, J., 2011. Direct Solar Energy, in: Edenhofer, O., Pichs-Madruga, R., Sokona, Y., Seyboth, K., Kadner, S., Zwickel, T., Eickemeier, P., Hansen, G., Schlömer, S., von Stechow, C., Matschoss, P. (Eds.), Renewable Energy Sources and Climate Change Mitigation: Special Report of the Intergovernmental Panel on Climate Change. Cambridge University Press, Cambridge, pp. 333–400. https://doi.org/DOI: 10.1017/CBO9781139151153.007

Babarit, A., 2015. A database of capture width ratio of wave energy converters. Renew Energy 80, 610–628. https://doi.org/10.1016/j.renene.2015.02.049

Boccotti, P., 2007. Caisson breakwaters embodying an OWC with a small opening—Part I: Theory. Ocean Engineering 34, 806–819. https://doi.org/10.1016/J.OCEANENG.2006.04.006

Boccotti, P., 2003. On a new wave energy absorber. Ocean Engineering 30, 1191–1200. https://doi.org/10.1016/S0029-8018(02)00102-6

Boccotti, P., Filianoti, P., Fiamma, V., Arena, F., 2007. Caisson breakwaters embodying an OWC with a small opening—Part II: A small-scale field experiment. Ocean Engineering 34, 820–841. https://doi.org/10.1016/J.OCEANENG.2006.04.016

Buccino, M., Vicinanza, D., Salerno, D., Banfi, D., Calabrese, M., 2015. Nature and magnitude of wave loadings at Seawave Slot-cone Generators. Ocean Engineering 95, 34–58. https://doi.org/10.1016/J.OCEANENG.2014.11.038

Chum, H., Faaij, A., Moreira, J., Berndes, G., Dhamija, P., Dong, H., Gabrielle, B., Eng, A.G., Lucht, W., Mapako, M., Cerutti, O.M., McIntyre, T., Minowa, T., Pingoud, K., Bain, R., Chiang, R., Dawe, D., Heath, G., Junginger, M., Patel, M., Yang, J., Warner, E., Paré, D., Ribeiro, S.K., 2011. Bioenergy, in: Edenhofer, O., Pichs-Madruga, R., Sokona, Y., Seyboth, K., Kadner, S., Zwickel, T., Eickemeier, P., Hansen, G., Schlömer, S., von Stechow, C., Matschoss, P. (Eds.), Renewable Energy Sources and Climate Change Mitigation: Special Report of the Intergovernmental Panel on Climate Change. Cambridge University Press, Cambridge, pp. 209–332. https://doi.org/DOI: 10.1017/CBO9781139151153.006

CorPower Ocean [WWW Document], n.d. . https://corpowerocean.com/.

Deng, Z., Huang, Z., Law, A.W.K., 2014. Wave power extraction from a bottom-mounted oscillating water column converter with a V-shaped channel. Proceedings of the Royal Society A: Mathematical, Physical and Engineering Sciences 470. https://doi.org/10.1098/rspa.2014.0074

DiPippo, R., 2015. Geothermal power plants: Evolution and performance assessments. Geothermics 53, 291–307. https://doi.org/10.1016/J.GEOTHERMICS.2014.07.005

DU HONG, B.D., Le, H.T., 2021. Improving efficiency in power production and transmission for offshore solar farms using bifacial panel design and hvdc. WSEAS Transactions on Power Systems 16. https://doi.org/10.37394/232016.2021.16.17

Evans, D. V., Porter, R., 1995. Hydrodynamic characteristics of an oscillating water column device. Applied Ocean Research 17, 155–164. https://doi.org/10.1016/0141-1187(95)00008-9

Falcão, A.F. de O., 2010. Wave energy utilization: A review of the technologies. Renewable and Sustainable Energy Reviews 14, 899–918. https://doi.org/10.1016/J.RSER.2009.11.003

Falcão, A.F.O., Henriques, J.C.C., 2016. Oscillating-water-column wave energy converters and air turbines: A review. Renew Energy. https://doi.org/10.1016/j.renene.2015.07.086

Falcão, A.F.O., Henriques, J.C.C., 2014. Model-prototype similarity of oscillating-water-column wave energy converters. International Journal of Marine Energy 6, 18–34. https://doi.org/10.1016/j.ijome.2014.05.002

Falcão, A.F.O., Henriques, J.C.C., Gato, L.M.C., 2016. Air turbine optimization for a bottom-standing oscillating-water-column wave energy converter. J Ocean Eng Mar Energy 2, 459–472. https://doi.org/10.1007/s40722-016-0045-7

Falcao, Sarmento, Gato, Brito-Melo, 2020. The Pico OWC wave power plant_ Its lifetime from conception to closure 1986–2018.

Faltinsen, O., 1990. Sea Lods on Ships and Offshore Structures.

Fu, L., Wang, R., Ning, D., Mayon, R., 2023. Numerical investigation on the hydrodynamic performance of a land-based OWC system with multi-chamber modules. Applied Ocean Research 141. https://doi.org/10.1016/j.apor.2023.103801

Gang, A., Guo, B., Hu, Z., Hu, R., 2022. Performance analysis of a coast – OWC wave energy converter integrated system. Appl Energy 311, 118605. https://doi.org/10.1016/J.APENERGY.2022.118605

Giorgi, G., Gomes, R.P.F., Henriques, J.C.C., Gato, L.M.C., Bracco, G., Mattiazzo, G., 2020. Detecting parametric resonance in a floating oscillating water column device for wave energy conversion: Numerical simulations and validation with physical model tests. Appl Energy 276, 115421. https://doi.org/10.1016/J.APENERGY.2020.115421

Heath, T. V, 2012. A review of oscillating water columns, in: Philosophical Transactions of the Royal Society A: Mathematical, Physical and Engineering Sciences. pp. 235–245. https://doi.org/10.1098/rsta.2011.0164

Hussain, A., Arif, S.M., Aslam, M., 2017. Emerging renewable and sustainable energy technologies: State of the art. Renewable and Sustainable Energy Reviews 71, 12–28. https://doi.org/10.1016/J.RSER.2016.12.033

Ibarra-Berastegi, G., Sáenz, J., Ulazia, A., Serras, P., Esnaola, G., Garcia-Soto, C., 2018. Electricity production, capacity factor, and plant efficiency index at the Mutriku wave farm (2014–2016). Ocean Engineering 147, 20–29. https://doi.org/10.1016/J.OCEANENG.2017.10.018

IEA, 2021. Electricity Information: Overview.

Khare, V., Chaturvedi, P., Mishra, M., 2023. Solar energy system concept change from trending technology: A comprehensive review. e-Prime - Advances in Electrical Engineering, Electronics and Energy 4, 100183. https://doi.org/10.1016/J.PRIME.2023.100183

Kofoed, J.P., Frigaard, P., Friis-Madsen, E., Sørensen, H.C., 2006. Prototype testing of the wave energy converter wave dragon. Renew Energy 31, 181–189. https://doi.org/10.1016/J.RENENE.2005.09.005

Kumar, K., Saini, R.P., 2022. A review on operation and maintenance of hydropower plants. Sustainable Energy Technologies and Assessments 49, 101704. https://doi.org/10.1016/J.SETA.2021.101704

Lange, M.A., 2013. Renewable Energy and Water Resources. Climate Vulnerability: Understanding and Addressing Threats to Essential Resources 3, 149–166. https://doi.org/10.1016/B978-0-12-384703-4.00320-8

Lewis, A., Estefen, S., Huckerby, J., Lee, K.S., Musial, W., Pontes, T., Torres-Martinez, J., Bharathan, D., Hanson, H., Heath, G., Louis, F., Scråmestø, S.Ø., Abdulla, A., Moreno, J.M., You, Y., 2011. Ocean Energy, in: Edenhofer, O., Pichs-Madruga, R., Sokona, Y., Seyboth, K., Kadner, S., Zwickel, T., Eickemeier, P., Hansen, G., Schlömer, S., von Stechow, C., Matschoss, P. (Eds.), Renewable Energy Sources and Climate Change Mitigation: Special Report of the Intergovernmental Panel on Climate Change. Cambridge University Press, Cambridge, pp. 497–534. https://doi.org/DOI: 10.1017/CBO9781139151153.010

Li, G., Zhu, W., 2023. Tidal current energy harvesting technologies: A review of current status and life cycle assessment. Renewable and Sustainable Energy Reviews 179, 113269. https://doi.org/10.1016/J.RSER.2023.113269

Linton, C.M.., McIver, P.., 2001. Handbook of mathematical techniques for wave/structure interactions. Chapman & Hall/CRC.

Lovas, S., Mei, C.C., Liu, Y., 2010. Oscillating water column at a coastal corner for wave power extraction. Applied Ocean Research 32, 267–283. https://doi.org/10.1016/j.apor.2010.06.004

Mansouri, A., Magri, A. El, Lajouad, R., Myasse, I. El, Younes, E.K., Giri, F., 2023. Wind energy based conversion topologies and maximum power point tracking: A comprehensive review and analysis. e-Prime - Advances in Electrical Engineering, Electronics and Energy 6, 100351. https://doi.org/10.1016/J.PRIME.2023.100351

Martins-Rivas, H., Mei, C.C., 2009. Wave power extraction from an oscillating water column at the tip of a breakwater. J Fluid Mech 626, 395–414. https://doi.org/10.1017/S0022112009005990

Michele, S., Renzi, E., Perez-Collazo, C., Greaves, D., Iglesias, G., 2019. Power extraction in regular and random waves from an OWC in hybrid wind-wave energy systems. Ocean Engineering 191. https://doi.org/10.1016/j.oceaneng.2019.106519

Mørk, G., Barstow, S., Kabuth, A., Pontes, M.T., 2010. Assessing the global wave energy potential, in: Proceedings of the International Conference on Offshore Mechanics and Arctic Engineering - OMAE. pp. 447–454. https://doi.org/10.1115/OMAE2010-20473

Ning, D., Fu, L., Zhou, Y., Mayon, R., Zhang, Y., 2024. Hydrodynamic performance of a land-based multi-chamber OWC wave energy capture system: An experimental study. Coastal Engineering 190, 104510. https://doi.org/10.1016/J.COASTALENG.2024.104510

Ning, D., Zhou, Y., Zhang, C., 2018. Hydrodynamic modeling of a novel dual-chamber OWC wave energy converter. Applied Ocean Research 78, 180–191. https://doi.org/10.1016/j.apor.2018.06.016

O'Sullivan, D., Griffiths, J., Egan, M.G., Lewis, A.W., 2011. Development of an electrical power take off system for a sea-test scaled offshore wave energy device. Renew Energy 36, 1236–1244. https://doi.org/10.1016/J.RENENE.2010.10.007

Palma, G., Contestabile, P., Zanuttigh, B., Formentin, S.M., Vicinanza, D., 2020. Integrated assessment of the hydraulic and structural

performance of the OBREC device in the Gulf of Naples, Italy. Applied Ocean Research 101, 102217. https://doi.org/10.1016/J.APOR.2020.102217

Pecher, A., Le Crom, I., Kofoed, J., Neumann, F., Azevedo, E., 2013. Performance Assessment of the Pico OWC Power Plant Following the Equimar Methodology, in: Proceedings of the International Offshore and Polar Engineering Conference. pp. 548–556.

Pelamis Wave Power [WWW Document], n.d. . https://www.emec.org.uk/about-us/wave-clients/pelamis-wave-power/.

Penalba, M., Giorgi, G., Ringwood, J. V., 2017. Mathematical modelling of wave energy converters: A review of nonlinear approaches. Renewable and Sustainable Energy Reviews 78, 1188–1207. https://doi.org/10.1016/J.RSER.2016.11.137

Pérez-Collazo, C., Greaves, D., Iglesias, G., 2015. A review of combined wave and offshore wind energy. Renewable and Sustainable Energy Reviews 42, 141–153. https://doi.org/10.1016/J.RSER.2014.09.032

Pires, A.L.G., Junior, P.R., Morioka, S.N., Rocha, L.C.S., Bolis, I., 2022. Main trends and criteria adopted in economic feasibility studies of offshore wind energy: A systematic literature review. Energies (Basel). https://doi.org/10.3390/en15010012

Qian, K., Chen, L., Zhou, Y., Ning, D., 2024. Hydrodynamics of an offshore multi-chamber OWC wave energy converter. Energy 304, 132239. https://doi.org/10.1016/J.ENERGY.2024.132239

Reid, W. V., Ali, M.K., Field, C.B., 2020. The future of bioenergy. Glob Chang Biol 26. https://doi.org/10.1111/gcb.14883

Shadman, M., Estefen, S.F., Rodriguez, C.A., Nogueira, I.C.M., 2018. A geometrical optimization method applied to a heaving point absorber wave energy converter. Renew Energy 115, 533–546. https://doi.org/10.1016/J.RENENE.2017.08.055

Sharmin, T., Khan, N.R., Akram, M.S., Ehsan, M.M., 2023. A State-of-the-Art Review on Geothermal Energy Extraction, Utilization, and Improvement Strategies: Conventional, Hybridized, and Enhanced Geothermal Systems. International Journal of Thermofluids 18, 100323. https://doi.org/10.1016/J.IJFT.2023.100323

Shi, X., Liang, B., Li, S., Zhao, J., Wang, J., Wang, Z., 2024. Wave energy resource classification system for the China East Adjacent Seas based on multivariate clustering. Energy 299, 131454. https://doi.org/10.1016/J.ENERGY.2024.131454

Silva, S.N., Castillo, J.Á. del, 2021. An Approach of the Hydropower: Advantages and Impacts. A Review. Journal of Energy Research and Reviews 10–20. https://doi.org/10.9734/jenrr/2021/v8i130201

Skilhagen, S.E., 2010. Osmotic power — a new, renewable energy source. Desalination Water Treat 15, 271–278. https://doi.org/10.5004/DWT.2010.1759

Spanò, A.S., Malara, G., Arena, F., 2024. Response of an Oscillating Water Column spanning a circle sector and embedded in a circular platform. Ocean Engineering 309. https://doi.org/10.1016/j.oceaneng.2024.118389

Thomson, R.C., Chick, J.P., Harrison, G.P., 2019. An LCA of the Pelamis wave energy converter. International Journal of Life Cycle Assessment 24. https://doi.org/10.1007/s11367-018-1504-2

Vicinanza, D., Di Lauro, E., Contestabile, P., Gisonni, C., Lara, J., Losada, I.J., 2019. Review of Innovative Harbor Breakwaters for Wave-Energy Conversion. J Waterw Port Coast Ocean Eng 145. https://doi.org/10.1061/(ASCE)WW.1943-5460.0000519

Wu, B., Chen, T., Jiang, J., Li, G., Zhang, Y., Ye, Y., 2018. Economic assessment of wave power boat based on the performance of “Mighty Whale” and BBDB. Renewable and Sustainable Energy Reviews 81, 946–953. https://doi.org/10.1016/J.RSER.2017.08.051

Zheng, S., Zhang, Y., Iglesias, G., 2019. Coast/breakwater-integrated OWC: A theoretical model. Marine Structures 66, 121–135. https://doi.org/10.1016/j.marstruc.2019.04.001

Zheng, S., Zhu, G., Simmonds, D., Greaves, D., Iglesias, G., 2020. Wave power extraction from a tubular structure integrated oscillating water column. Renew Energy 150, 342–355. https://doi.org/10.1016/j.renene.2020.01.008

Zhou, Y., Zhang, C., Ning, D., 2018. Hydrodynamic investigation of a concentric cylindrical OWC wave energy converter. Energies (Basel) 11. https://doi.org/10.3390/en11040985